Lewy pathology in Parkinson's disease consists of crowded organelles and lipid membranes

Sarah H. Shahmoradian [1,12], Amanda J. Lewis [1], Christel Genoud[2], Jürgen Hench[3], Tim E. Moors[4], Paula P. Navarro[1], Daniel Castaño-Díez[1], Gabriel Schweighauser[3], Alexandra Graff-Meyer[2], Kenneth N. Goldie[1], Rosmarie Sütterlin[1], Evelien Huisman[4], Angela Ingrassia[4], Yvonne de Gier[4], Annemieke J. M. Rozemuller[5], Jing Wang[1], Anne De Paepe[6], Johannes Erny[7], Andreas Staempfli[7], Joerg Hoernschemeyer[7], Frederik Großerüschkamp[8], Daniel Niedieker[8], Samir F. El-Mashtoly [8], Marialuisa Quadri[9], Wilfred F. J. Van IJcken [10], Vincenzo Bonifati[9], Klaus Gerwert[8], Bernd Bohrmann[11], Stephan Frank[3], Markus Britschgi[11,13], Henning Stahlberg [1,13]*, Wilma D. J. Van de Berg [4,13]* and Matthias E. Lauer [6,13]*

Parkinson's disease, the most common age-related movement disorder, is a progressive neurodegenerative disease with unclear etiology. Key neuropathological hallmarks are Lewy bodies and Lewy neurites: neuronal inclusions immunopositive for the protein α-synuclein. In-depth ultrastructural analysis of Lewy pathology is crucial to understanding pathogenesis of this disease. Using correlative light and electron microscopy and tomography on postmortem human brain tissue from Parkinson's disease brain donors, we identified α-synuclein immunopositive Lewy pathology and show a crowded environment of membranes therein, including vesicular structures and dysmorphic organelles. Filaments interspersed between the membranes and organelles were identifiable in many but not all α-synuclein inclusions. Crowding of organellar components was confirmed by stimulated emission depletion (STED)-based super-resolution microscopy, and high lipid content within α-synuclein immunopositive inclusions was corroborated by confocal imaging, Fourier-transform coherent anti-Stokes Raman scattering infrared imaging and lipidomics. Applying such correlative high-resolution imaging and biophysical approaches, we discovered an aggregated protein–lipid compartmentalization not previously described in the Parkinsons' disease brain.

Lewy bodies (LB) have been recognized as the main pathological hallmark of Parkinson's disease (PD) and dementia with Lewy Bodies (DLB) following their microscopic discovery over 100 years ago. The protein α-synuclein (αSyn) has been found to be a major component of LB and is considered to play a central role in their formation and of other Lewy pathologies including LB, pale bodies and Lewy neurites (LN)[1]. The morphology of LB revealed by light microscopy varies depending on their location in the brain (brainstem, limbic or neocortical)[2,3], may reflect maturation stage and genetic background, and their biochemical and proteomic composition is known to be complex[2,4]. The morphology of LN, displaying the same αSyn immunohistochemical staining profile[5,6] as those found in the neuronal cell bodies, also varies between brainstem and (sub)cortical brain regions[7].

The processes by which Lewy pathology arise and their roles in neurodegeneration remain elusive. The current, leading hypothesis in PD research proposes that intraneuronal αSyn first forms as abnormal oligomers, possibly induced by extracellular pathogenic αSyn aggregates that were taken up and subsequently transforms into β-sheet rich amyloid fibrils, which are the basis of the LB[8]. Transmission electron microscopy (TEM) carried out on sarcosyl-insoluble fractions of brain tissue extracts or formalin-fixed, de-paraffinized and resin-embedded postmortem brain tissue of patients with PD or DLB, revealed the ultrastructure of LB as filaments immunoreactive for αSyn[3,9]. By contrast, evidence from ultrastructural studies based on neuroanatomical localization point to an electron-dense core and granular features[10]. Proteome studies have shown that LB consists of more than 300 proteins, of which approximately 90 have been confirmed by immunohistochemistry in various postmortem studies and are associated with αSyn, protein degradation systems, molecular chaperones or axonal damage[2]. Current literature about the nature of Lewy pathology is in several aspects still incomplete and requires validation to make proper conclusions about pathogenesis and progression of PD.

A clearer understanding of the building blocks of Lewy pathology is therefore necessary.

The discovery that recombinant αSyn can form filaments in vitro has most likely influenced the search for a filamentous type of αSyn-immunopositive inclusion within human brain tissue and extracts in past ultrastructural studies. Until now, no ultrastructural study exists using postmortem brain tissue from multiple PD donors that has used unequivocal identification of Lewy pathology from an unbiased correlative microscopy approach. With the advent of modern technologies for electron microscopy such as energy filters, direct electron detectors and drift-correcting software for tomography, we now have the possibility to obtain a clearer and more accurate picture of the three-dimensional (3D) structure of such αSyn-immunopositive pathological inclusions, including the capability of distinguishing amyloid fibrils from lipid membranes. Such advanced TEM imaging can be done in correlation with light microscopy imaging.

Here, we present a 3D view of the structural components of 17 LB and LN in well-preserved brain tissue from five PD brain donors using correlative light and electron microscopy (CLEM). The correlative methods employed clearly show that while we are able to resolve filaments, we observe an abundance of crowded membranous material in Lewy pathology, with membranes appearing to originate from vesicles and fragmented organelles including mitochondria. Serial block-face scanning electron microscopy (SBFSEM), enabling visualization of a larger tissue volume at intermediate resolution as compared to CLEM, also revealed crowded organelles and membrane fragments in such aggregates, and a shell of mitochondria surrounding some of these inclusions. Correlative multi-labeling and stimulated emission depletion microscopy (STED) were employed to corroborate these assignments in brain tissue from 14 PD donors, including those used for CLEM, and demonstrated the crowding of αSyn, lipids, lysosomal structures and mitochondria in LB and LN. The presence of lipids in LB was confirmed by label-free compositional mapping methods and mass spectrometry. The nanoscale information obtained suggests that the membrane crowding observed in Lewy pathology is modulated by αSyn, and supports the hypothesis that impaired organellar trafficking contributes to PD pathogenesis[11].

Results

A CLEM approach was employed to identify Lewy pathology in advanced PD brain donors (Supplementary Table 1). By CLEM, we obtained a 3D view of the ultrastructure of 17 αSyn-immunopositive inclusions in neurons, three of which were identified as LN, within postmortem samples from five PD donors (Supplementary Table 2). The presence, distribution and morphology of Lewy pathology in the substantia nigra (SN) and hippocampal CA2 in these donors were determined by light microscopy of paraffin-embedded tissue sections immunostained for αSyn and illustrated the accumulation of αSyn in these brain regions (Supplementary Fig. 1a–h). CLEM (Supplementary Figs. 2–9) was performed using adjacent tissue blocks prepared at autopsy in parallel from the same tissue sample; αSyn-immunoreactive inclusions were identified by histological staining followed by light microscopy and 3D TEM tomograms (Figs. 1–3, Supplementary Figs. 2, 3 and 5 and Supplementary Videos 1–19) and two-dimensional (2D) TEM images (Figs. 4–6 and Supplementary Figs. 7–9) were recorded from adjacent tissue sections (that is, regions maximally 450 nm above or below in the block).

Of all Lewy pathology we identified using CLEM, we observed only a single αSyn-immunopositive inclusion comprising a proteinaceous core, radiating filaments and organelles at the periphery, localised among neuromelanin-containing organelles in the SN (Fig. 1d, Supplementary Fig. 7, Supplementary Video. 4 and Supplementary Table 2, Donor C-PD). Also within neuromelanin-containing

organelles in the SN of two separate brain donors, we observed strongly αSyn-immunopositive inclusions containing abundant aggregates of mitochondria, numerous lipid vesicles and worm-like tubulovesicular structures (Supplementary Fig. 8, Donor D-PD and Supplementary Fig. 9, Donor E-PD, pink arrowheads), interspersed with randomly oriented filaments (Supplementary Figs. 8 and 9, blue arrowheads). In two αSyn-immunopositive inclusions not co-localised with neuromelanin yet also found in the SN of Donors D-PD and E-PD, we observed both abundant vesicular structures and structures with filamentous appearance. In Donor D-PD, we observed abundant tubulovesicular structures (Fig. 5, pink arrowheads) interspersed with randomly oriented filaments (Fig. 5, blue arrowheads). In Donor E-PD, we observed a single αSyn-immunopositive inclusion comprising autophagic vacuolar-like structures (membrane-enclosed, 'empty' vesicles) similar to what was observed in a LN (Fig. 4), vesicles with a ruffled border, distorted vesicles, vesiculotubular structures (Fig. 6, pink arrowheads) and randomly oriented filaments (Fig. 6, blue arrowheads).

Only three αSyn-immunopositive inclusions among 17 appeared to consist primarily of filamentous structures (Fig. 1d and Supplementary Fig. 6d,e). Overall, the majority of αSyn inclusions appear to mainly consist of a multitude of membranes including crowded organelles (Figs. 1a–c, 2–8, Supplementary Fig. 6a–c,e,f and Supplementary Videos. 1–3, 5–7, 9–17, 20 and 21). The TEM tomograms revealed mitochondria and numerous cellular organelles clearly visible at the periphery and interior of the inclusions. Densely compacted membranous structures, tubulovesicular structures, distorted vesicles and haphazardly distributed filaments were also visible.

Besides abundant vesicular structures scattered throughout the αSyn-immunopositive inclusions, dense 'dark' L-shaped structures resembling stacks of compacted membrane sheets with a membrane layer spacing of ~6 nm were distinguished (Fig. 1a–c, Supplementary Fig. 6a–c,e yellow arrowheads and Supplementary Videos. 1–3, 5–7 and 9). They cannot be attributed to myelin, which has an average membrane spacing of 10.7 nm in the central nervous system[12]. Furthermore, vesicular structures of varying electron density (Fig. 2a–d and Supplementary Videos 11–15) were observed within the inclusions in higher magnification TEM tomograms. These structures are reminiscent of lysosomes and autophagosomes[13]. In addition, the tomograms reveal distorted mitochondria (Fig. 1 and Supplementary Fig. 6, white arrowheads; Fig. 2c, dotted ellipse; Fig. 3b, black arrowhead; Fig. 8a–c and Supplementary Figs. 8 and 9) and other features (Fig. 2c, pink arrowhead) that resemble the disk-like structures reported for in vitro-generated αSyn-lipoprotein particles examined by cryogenic electron microscopy[14]. These disk-like and tubulovesicular structures appear frequently in 2D TEM images of other αSyn-immunopositive structures in different brain donors (Figs. 5 and 6 and Supplementary Figs. 8 and 9, pink arrowheads) and within two regions of a LN in Donor E-PD (Fig. 4, pink arrowheads). Computational analysis of the vesicular structures (Fig. 2e) by subtomogram averaging revealed their 3D structure, indicating the presence of two basal planes as expected for membrane leaflets (Fig. 2f). As a control for the subtomogram averaging, neurofilaments present within a neurite from a non-neurological control human brain (Fig. 2g) were similarly analyzed and shown to consist of a rod-like structure, as previously described (Fig. 2h)[15].

The same CLEM strategy (Supplementary Figs. 2–5) was applied to precisely locate and visualize the ultrastructure of αSyn-immunopositive inclusions within neurites (Figs. 3 and 4 and Supplementary Figs. 5 and 6f). A 3D TEM tomogram of one such LN in Donor B-PD contained disordered neurofilaments interspersed with vesicular structures reminiscent of mitochondria or remnants thereof (Fig. 3a, blue arrowheads), autophagosomes[13] (Fig. 3a,b, white asterisk), and sporadically a dense-core vesicle (Fig. 3a, black arrowhead). A transition from order to disorder can be seen

Mitochondria
Undefined proteinacious inclusions
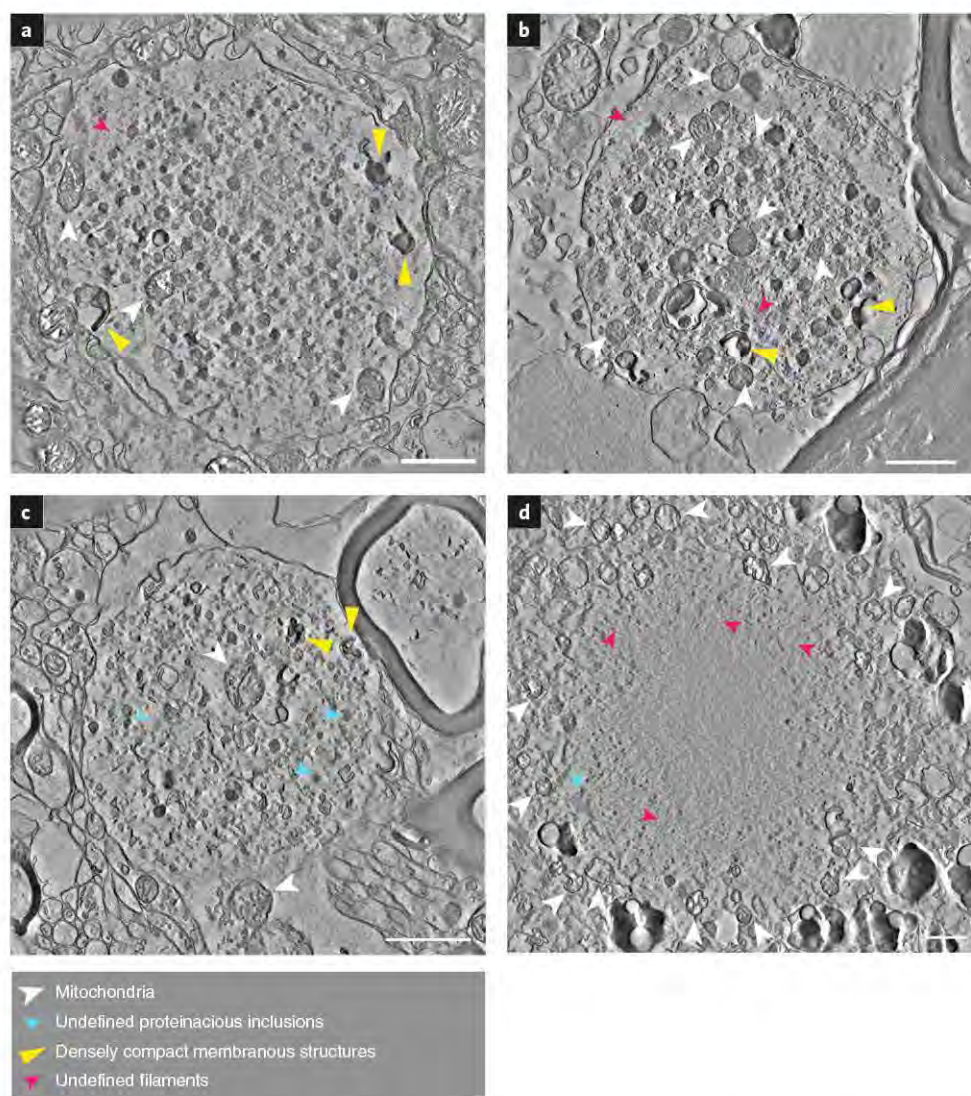Densely compact membranous structures
Undefined filaments

Fig. 1 | Lewy pathology shows abundant membranous structures, abnormal organelles and vesicles. Projections of the central 20 slices of each reconstructed 3D tomogram are shown for each αSyn-immunopositive inclusion found by CLEM and surrounding cellular milieu. Feature details (arrowheads) are tabulated in Supplementary Table 2. Additional αSyn-immunopositive Lewy pathological inclusions are shown in Figs. 3–6 and Supplementary Figs. 5–9. Donor identities are shown in Supplementary Table 1. **a**, Donor A-PD (Supplementary Video 1). **b**, Donor B-PD (Supplementary Video 2). **c**, Donor D-PD (Supplementary Video 3). **d**, Donor C-PD (Supplementary Video 4). CLEM data shown in Supplementary Fig 3a. Scale bars, 1 μm.

where structures resembling neurofilaments[15] (Fig. 3b, white arrowheads) appear to become disrupted over the length of the neurite (Supplementary Videos 16 and 17). Such disorganization was not observed in brain samples of an aged non-neurological control subject; the paths of neurofilaments are far more sharply delineated (Fig. 3c,d), and mitochondria within the neurites exhibit intact cristae (Fig. 3d, black asterisk and Supplementary Videos 18 and 19). Another 3D TEM tomogram of a separate αSyn-immunopositive LN (Supplementary Fig. 6f) in a different donor (Donor D-PD) was shown to consist entirely of vesicles and membranous structures. A third LN, found in Donor E-PD, contained abundant tubulovesicular structures interspersed with filaments (Fig. 4).

SBFSEM of corresponding tissue from one of the same brain donors (Donor B-PD) as used for CLEM, provided 3D reconstructions of αSyn-immunopositive inclusions across volumes spanning tens of microns (Fig. 7 and Supplementary Video 20), resulting in a comprehensive 3D view of these aggregates in tissue at a spatial resolution of ~16 nm. The SBFSEM data revealed cytoplasmic inclusions of aggregated intracellular material (Fig. 7 and Supplementary

Video 20) and the presence of many mitochondria (Fig. 7a,b, orange arrows) and other organelles resembling autophagosomes and lysosomes (Fig. 7a,b, aqua arrows), in agreement with Nixon et al.[13]. A representative inclusion identified by SBFSEM was imaged at higher resolution (100–200 nm) by correlative TEM to define their ultrastructure more clearly. The TEM showed the analyzed inclusions to comprise membrane fragments (Fig. 8), with clearly distinguishable lipid bilayers similar to those in membranes of intact organelles. One inclusion also exhibited dysmorphic, elongated mitochondria at its immediate periphery, either clustered with other membrane fragments and vesicles (Fig. 8a) or encased in distinct cellular compartments (Fig. 8b) in a state of what appeared to be partial degradation. Other mitochondria were more centrally located in the aggregate and surrounded by membrane fragments (Fig. 8c).

Clusters of membrane fragments, vesicles and structures resembling dysmorphic mitochondria (Fig. 8f), omegasomes (autophagosome precursors; Fig. 8d,e, black arrowheads) and lysosomes (Fig. 8d,e, pink arrowheads), were located toward the center of the inclusion. Filamentous structures were observed in regions within
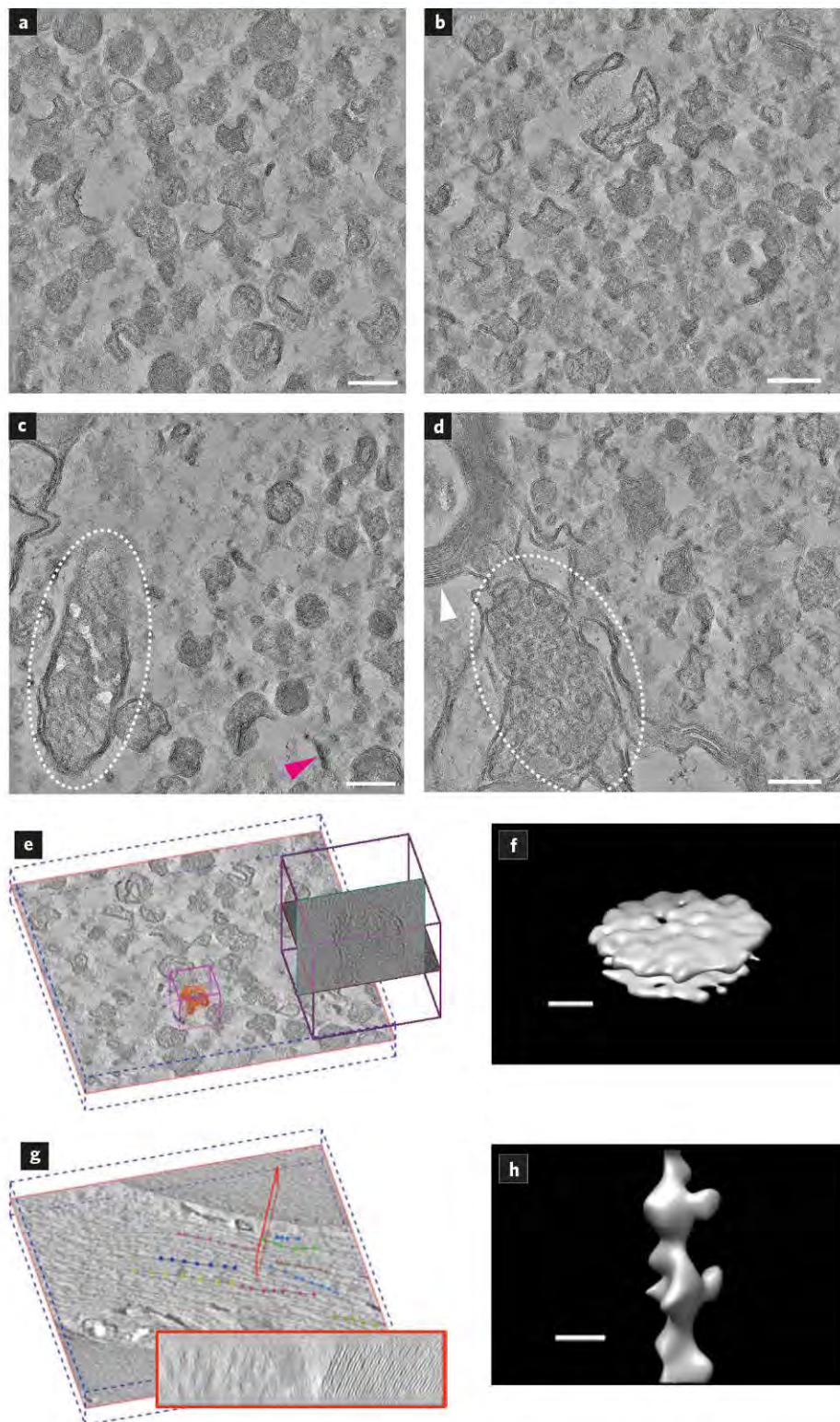
Fig. 2 | Electron tomography and subtomogram averaging reveal membranous nature of Lewy pathology. Projections of the central 60 slices of each reconstructed 3D tomogram are shown for each subregion of αSyn-immunopositive inclusion shown in **a–d** for Donor A-PD. **a,b,** Inner region of the inclusion as shown in Fig. 1a (**a**) and in Supplementary Fig. 6a (**b**). **c,** Edge of the inclusion as shown in Fig. 1a. White oval, distorted mitochondrion; pink arrow, representative disc-like membranous structure. More of such structures are visible in 3D; see Supplementary Videos 11–15. **d,** Edge of the inclusion as shown in Supplementary Fig. 6a. Cluster of vesicular structures in adjacent yet separate compartment to the inclusion is visible (white oval). **e,** Z-orthoslice in a tomogram from an inclusion, the region selected for subtomogram averaging (pink box) and the locations of sampled subvolumes at high intensity points (red). **f,** Subtomogram average for the sampled densities in the inclusion show a membrane structure with the two leaflets separated by the typical spacing of lipid bilayer. **g,** Z-orthoslice in a tomogram from a neurite of a non-neurological, age-matched control brain donor. The red box indicates a cross-section showing myelin sheaths (right) and filaments (left) within the neurite. **h,** Subtomogram average for the sampled densities along the dotted lines in **g** show a filamentous structural signature. Scale bars: **a–d,** 200 nm; **f,h,** 10 nm.

the same tissue section but distal to the LB (Fig. 8h,i). Furthermore, most mitochondria within the inclusion (Fig. 8a–d) were dysmorphic compared to mitochondria found within the cytoplasm of intact cells of the same tissue section, yet distal to the inclusion (Fig. 8g,i).

To clarify the identities and distributions of vesicular structures found within Lewy pathology, multiple labeling experiments followed by 3D gated STED microscopy was applied (n = 14 PD donors in total). Lysosomal and mitochondrial markers were chosen for STED investigations since lysosomal-type structures and mitochondria were observed in the αSyn-immunopositive inclusions using electron microscopy. Morphologies of LB/LN were classified based on the presence or absence of an outer layer of αSyn phosphorylated at Serine 129 (p-αSyn). LB with a uniform distribution of p-αSyn reactivity throughout the structure were observed in hippocampus and SN, and showed widespread immunoreactivity for LAMP-1 as well as VDAC1-immunopositive mitochondria (Supplementary Fig. 10), along with some inclusions showing empty vacuoles that may represent autophagic vacuolar-like structures (membrane-enclosed, 'empty' vesicles) (representative one shown in Supplementary Fig. 10,f,i,j). The presence of empty vacuoles in these inclusions by STED bears similarity to separate αSyn-immunopositive inclusions identified by CLEM (Figs. 4 and 6). LB and LN with an outer layer of p-αSyn immunoreactivity were observed predominantly in the SN, and displayed a peripheral clustering of VDAC1-immunopositive mitochondria (Fig. 7d,i,n, Supplementary Fig. 13 and Supplementary Video 21).

The STED images of LB with uniform distribution of p-αSyn support the CLEM data (Figs. 1, 2 and 4 and Supplementary Figs. 6, 8 and 9) and SBFSEM data (Fig. 7 and Supplementary Video 20) that demonstrate a relatively even distribution of lysosomal-type structures and mitochondria interspersed. In LB with a p-αSyn positive outer layer, we also observed a shell of mitochondria directly surrounding some of the inclusions (Fig. 7a,b), corroborating our SBFSEM data (Fig. 7 and Supplementary Video 20), correlative SBFSEM/TEM (Fig. 8) and 2D CLEM data (Fig. 6). Overall, the STED data generated on brain samples from 14 PD donors confirm that different Lewy inclusion morphologies (with and without an outer layer of p-αSyn) contain organelles or organellar remnants, including mitochondria and lysosomes.

To cross-validate the high lipidic content of αSyn-immunopositive inclusions as observed in our TEM tomograms, 10 µm-thick cryostat sections were collected from tissue blocks of the same SN region from the same brain donor (Donor B-PD, see Supplementary Table 1) and the CA2 region of the hippocampus obtained from another late stage PD brain donor (Donor A-PD, see Supplementary Table 1). These cryostat-cut tissue sections were then co-stained for lipids (Nile Red) and αSyn. In both cases, projections of the image stacks collected by confocal fluorescence microscopy showed co-localized staining of lipids and αSyn in the LB examined (Supplementary Fig. 11), supporting the concept of a high membrane content therein.

LB were examined by three additional methods to confirm the membranous lipid content shown by confocal fluorescence microscopy (Supplementary Fig. 11), and thus corroborate the presence of cellular or organellar membranes indicated by the electron microscopy data (Figs. 1a–c and 2–6 and Supplementary Figs. 6a–c,e,f, 8 and 9). The first method combined coherent anti-Stokes Raman scattering (CARS) with subsequent immunofluorescence staining and confocal laser scanning microscopy (CLSM) in correlative measurements. CARS is a nonlinear optical imaging method that allows the label-free identification of the chemical composition of lipids and proteins in tissue at a resolution of 300 nm. Cryostat sections cut from tissue blocks taken from the same brain regions of the brain donors as used for the electron and light microscopy studies were investigated, namely the CA2 region of Donor A-PD and the SN region of Donor B-PD. CARS detected a high lipid content throughout αSyn-labeled inclusions: in areas that showed a higher αSyn signal, we observed a higher
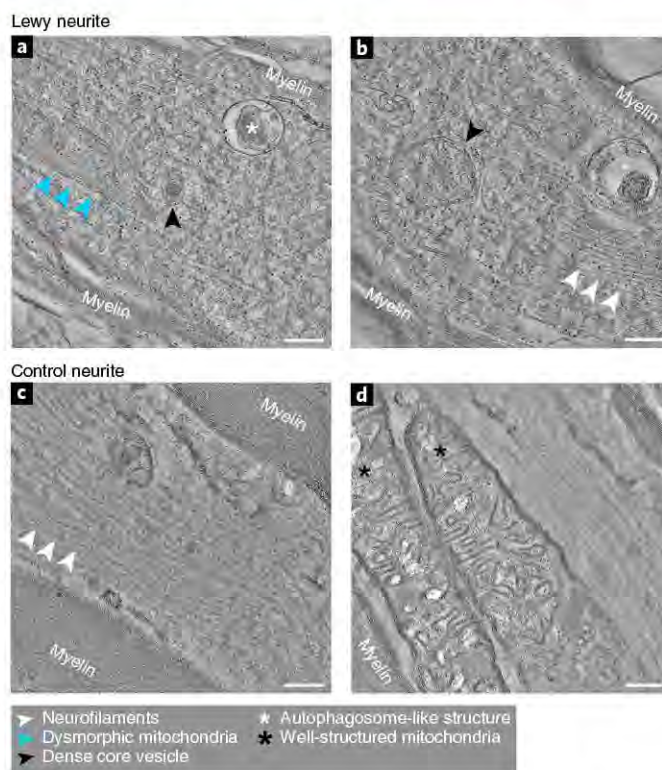
Lewy neurite

Control neurite

> Neurofilaments   ★ Autophagosome-like structure
> Dysmorphic mitochondria ✱ Well-structured mitochondria
> Dense core vesicle

Fig. 3 | Nigral Lewy neurite reveals disrupted cytoskeletal elements, dysmorphic mitochondria and autophagosome-like structures. Electron tomography of LN identified using CLEM from Donor B-PD SN. **a**, Inner region of the LN shown in the overview image Supplementary Fig. 5c (upper dotted red box) and Supplementary Video 16. Abnormally elongated and dysmorphic mitochondria are visible. **b**, Different inner region of the LN shown in Supplementary Fig. 5c (lower dotted red box) and Supplementary Video 17. **c,d**, Control neurites, **c**, Inner region of a normal neurite (Supplementary Video 18) in the brain of an age-matched control donor not diagnosed with neurological disease (Donor F-Control, Supplementary Table 1). Ordered neurofilaments are visible next to well-structured myelin sheath representing the enclosing axon. **d**, Inner region of a separate neurite (Supplementary Video 19) in the brain of the same donor as shown in **c**. **a,b**, Projection through the central 40 slices of the reconstructed 3D tomogram. **c,d**, Projection through the central 60 slices of the reconstructed 3D tomogram. Scale bars, 200 nm.

lipid signal as compared to the surrounding tissue (Supplementary Fig. 12a–d) in the correlative tissue sections.

The second method used to confirm the presence of lipids, combined high-definition Fourier transform infrared (FTIR) spectroscopic imaging with subsequent correlative immunofluorescence staining to detect αSyn and CLSM (FTIR–IF). FTIR imaging exploits the fact that the absorption of mid-infrared light waves by chemical bonds (for example, C=O, C–H, N–H) depends on the chemical environment of the bonds, that is, the presence and composition of specific biomolecules within cells or tissue (that is, lipids, protein and DNA). FTIR therefore does not require the use of labels. The FTIR-IF results confirmed that αSyn-immunoreactive inclusions are rich in lipids (Supplementary Fig. 12e–h). The CARS and FTIR lipid and protein profile of neurons in non-neurological controls showed less lipids and proteins than the surrounding tissue, whereas LB showed an increase in lipid and protein profile in the SN and CA2 (Supplementary Fig. 13). With these measurements, we showed that the increase in the lipid and protein signals in these inclusions were attributable to the actual inclusion itself.
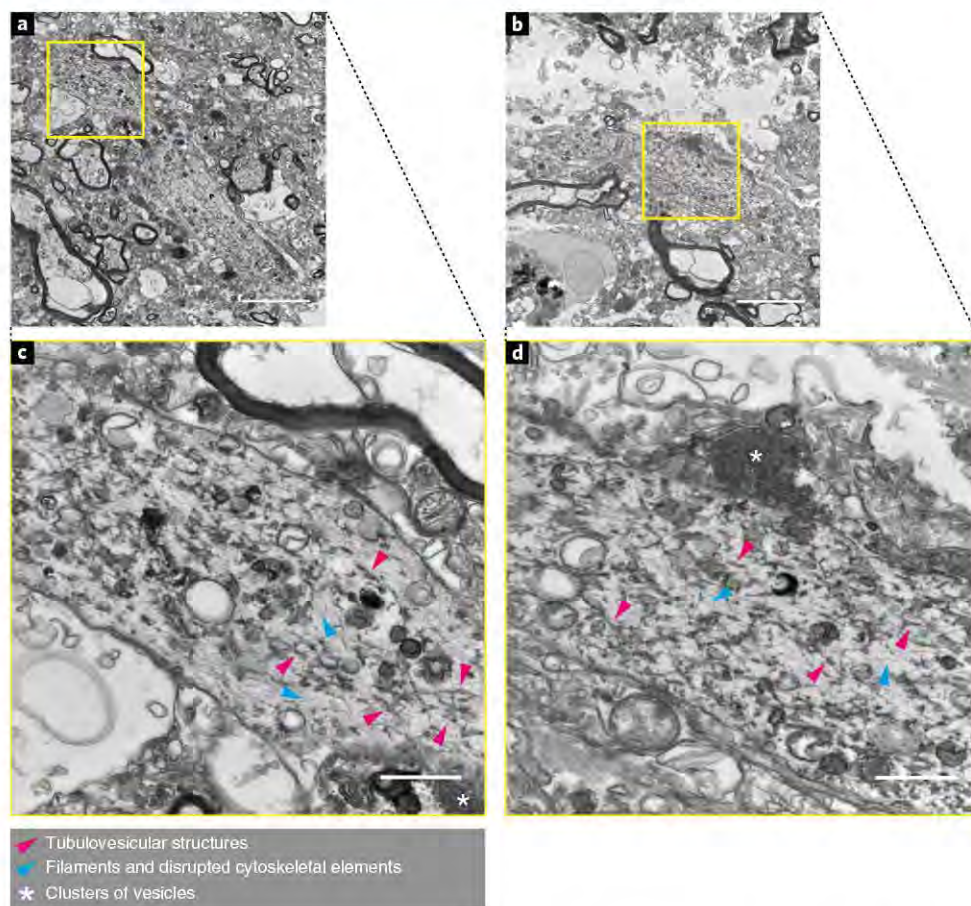
Fig. 4 | Nigral Lewy neurite revealing disrupted cytoskeletal elements, tubulovesicular, lysosome- and autophagosome-like structures. Electron tomography of a LN identified by CLEM from Donor E-PD SN. 2D images. **a,b,** Top part (**a**) and bottom part (**b**) of the LN as shown in Supplementary Fig. 5a,b. **c,d,** Inner region at higher magnification of the LN as shown in **a** and **b**, respectively. Autophagic vacuolar-like structures (membrane-enclosed, 'empty' vesicles), lysosomal structures such as lipofuscin (black and dark gray semi-circular structures) and structures resembling mitochondria are visible in addition to the annotated features. Scale bars: **a,b**, 5 μm; **c,d**, 1 μm.

Finally, liquid chromatography–mass spectrometry (LC–MS) and lipidomics analyses were applied to LB isolated by laser-capture microdissection microscopy (LCM). LB identified by αSyn immunostaining were extracted from 7 μm-thick cryostat-cut tissue sections of SN (~3,050 LB) and CA2 (~2,700 LB) of the same PD brain donors (Donors B-PD and A-PD, respectively, see Supplementary Table 1) using LCM. The subsequent analysis confirmed the high cell membrane related lipid content indicated by other methods, with the mass spectra showing strong peaks corresponding to sphingomyelin and phosphatidylcholine for αSyn-immunopositive inclusions isolated from both the SN and hippocampal CA2 sector (Supplementary Fig. 14b,c). Similar peaks were observed in myelin-rich/lipid-rich regions dissected from the corpus callosum of a non-neurological control brain donor, and cells of the dentate gyrus from the hippocampus of Donor A-PD (Supplementary Fig. 14a,d). The sphingomyelin/phosphatidylcholine profile is not specific for LB, which contain abundant membranes that originate from the cell itself; therefore, it is not surprising that their lipid profile would be similar.

These orthogonal methods confirm that Lewy pathology contain both αSyn and lipids in close proximity and show that they are rich in lipids found in other physiological and lipid-rich structures in the brain; for example, organellar membranes. They fully corroborate the interpretation of our microscopy data, confirming that Lewy pathology contains αSyn, lipids, lysosomes and mitochondria.

Discussion

By light microscopy, LB and LN are identified as αSyn-immunopositive intraneuronal inclusions with varying morphology. Our results using CLEM, SBFSEM and TEM to analyze αSyn-immunoreactive inclusions at the nanometer scale show that Lewy pathology in brain tissue of PD donors largely consists of a multitude of fragmented membranes, organelles and vesicles. Some (seven) consisted entirely of membranous material with very few to no distinguishable filaments (Figs. 1a–c and 2, Supplementary Fig. 6a–c,f and Supplementary Table 2), while filaments were observed as dispersed among membranous structures within other inclusions (Figs. 1, 4 and 6, Supplementary Figs. 7–9, blue arrowheads or blue asterix and Supplementary Table 2) and only three out of 17 inclusions contained filaments rather than abundant membranes and organelles (Supplementary Table 1, Fig. 1d and Supplementary Figs. 6d,e and 7). So far, the literature describes 'classical LB' imaged by electron microscopy as filaments in a spherically radiating focal architecture[9]. While we were able to observe such a morphology in 1 out of 17 analyzed LB/LN (Fig. 1d and Supplementary Fig. 7), we discovered in the well-preserved human tissue blocks from donors with PD that most of the αSyn-positive Lewy pathology analyzed by our correlative and multi-imaging approach consist of a crowded mix-up of organellar and membranous features. This also confirms the presence of varying morphology and heterogeneity of Lewy pathology on a nanoscale level.
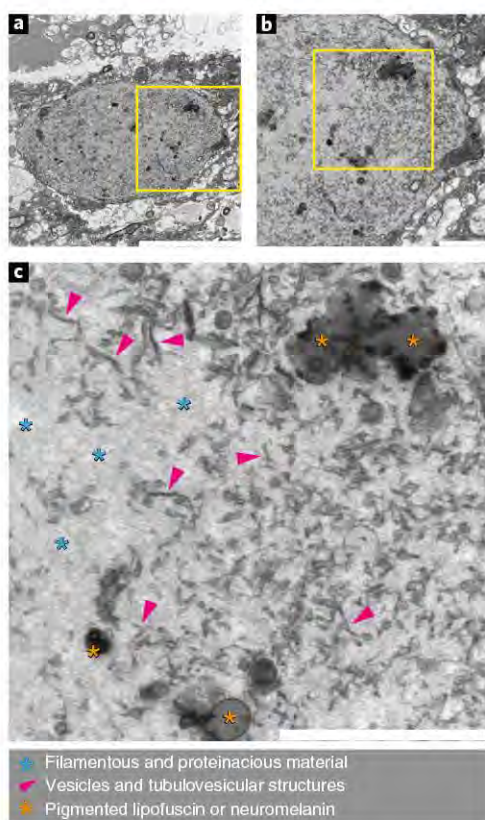
Fig. 5 | Lewy pathology consisting of abundant tubulovesicular structures. Structures identified by CLEM in Donor D-PD. CLEM data are shown in Supplementary Fig. 3h. **a–c**, 2D electron micrographs showing the ultrastructure of an αSyn-immunopositive inclusion at low magnification, in which it can be seen delimited by membrane (**a**), at increasingly higher magnification in **b,c** as indicated by the yellow boxes. Scale bars: **a**, 10 μm; **b,c**, 2 μm.

These findings support a key role for potentially damaged, distorted organelles in the formation of LB and LN, a major process in the pathogenesis of PD. Our criteria for identification of LB and LN are primarily based on the strong staining for LB509 (anti-αSyn), which is routinely used to identify Lewy pathology, and allowed distinguishing from other brain inclusions such as corpora amylacea[16] (Supplementary Fig. 1i–l). Given that each tissue section collected for light and electron microscopy was 100–200 nm in thickness, we could overlay the same tissue features very precisely in one section for light microscopy and the adjacent section for electron microscopy. Our CLEM approach assured that the spherical aggregates of similarly reported LB diameters (~4–25 μm)[9,17] at the indicated locations of LB found by light microscopy, correspond to the matching structures in electron microscopy.

Given the distinctive morphology of historically-identified LB within the monochrome and crowded cellular landscape by electron microscopy, our results help explain why in past studies only distinctly filamentous inclusions could be identified by electron microscopy alone. The other αSyn-immunopositive inclusions containing crowded membranes are more difficult to distinguish from the cellular background in TEM images alone, and can only be found when using CLEM.

Since our TEM tomograms capture the content of tissue sections spanning 100–200 nm in thickness, we can only report about the contents of these sections, which represent a fraction of each LB/LN. Based on the visibility of other filaments, we estimate our
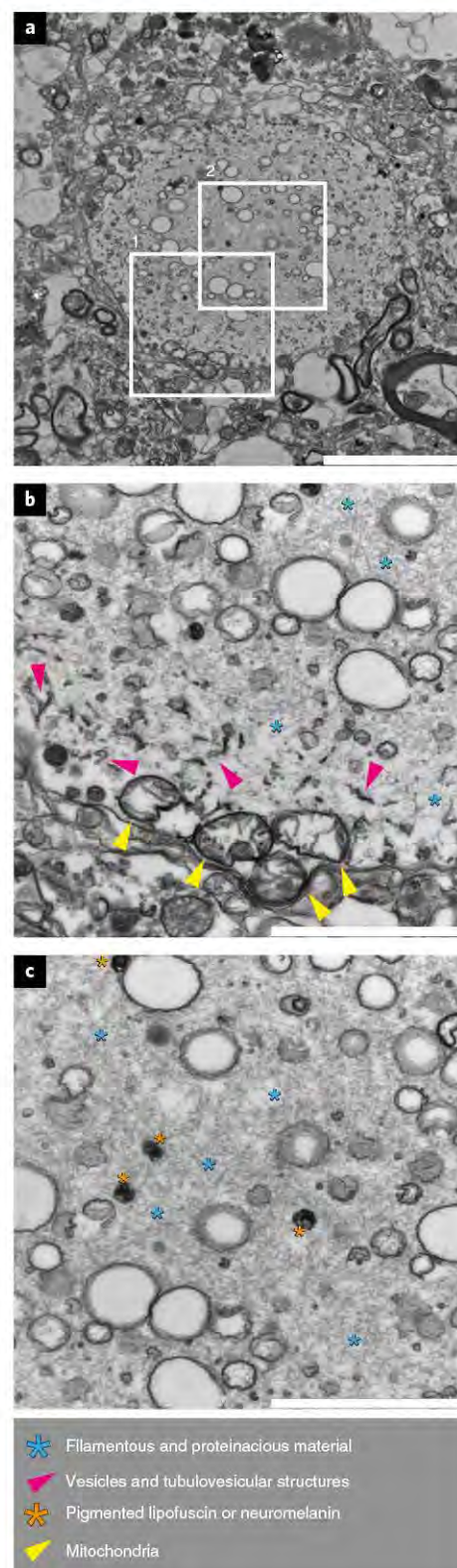
Fig. 6 | Lewy pathology consisting of abundant vesicular structures interspersed with filaments. Structure identified by CLEM in Donor E-PD. CLEM data are shown in Supplementary Fig. 3e. **a–c**, 2D electron micrographs showing the ultrastructure of an αSyn-immunopositive inclusion at low magnification (**a**) and higher magnification of boxed regions 1 (**b**) and 2 (**c**). Abundant autophagic vacuolar-like structures (membrane-enclosed, 'empty' vesicles) and vesicles with a ruffled border observed mainly in center. In addition to the other annotated features, abnormal mitochondria with few cristae are visible at the periphery. Scale bars: **a**, 5 μm; **b,c**, 2 μm.

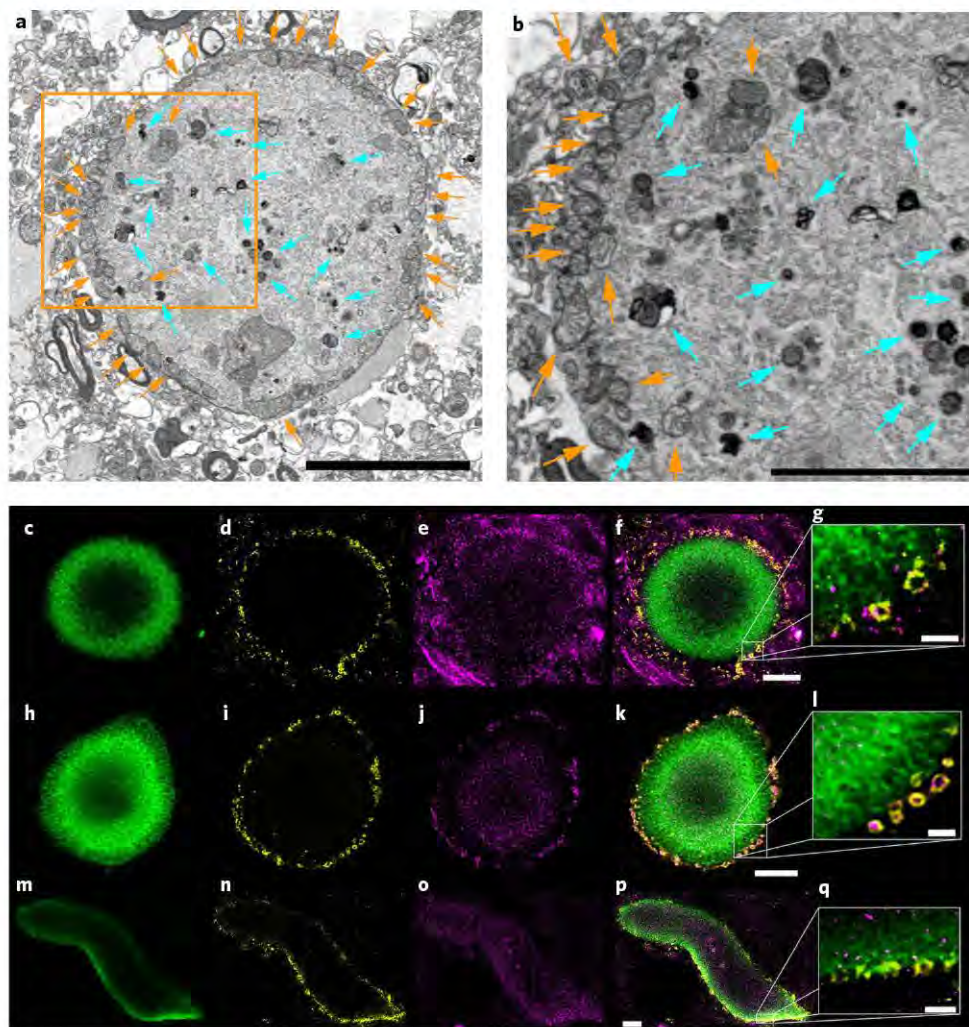**Fig. 7 | Subcellular features of Lewy pathology reveal the organelle distribution. a,** SBFSEM imaging of heavy-metal stained SN tissue in Donor B-PD showing a surrounding ring of mitochondria (orange arrows) and structures resembling lysosomes (aqua arrows) further within the inclusion. **b,** Enlarged view of the boxed region in **a**, similarly annotated. **c–q,** Microscopy of a separate inclusion in the same SN region of the same brain donor (Donor B-PD) (**c–g**), and Lewy pathology in the SN of Donor A-PD (**h–q**), showing the distribution of the marker for phosphorylated αSyn (pS129) (**c,h,m**), the marker for mitochondria (porin, also called VDAC1) (**d,i,n**), the marker for lysosomes (LAMP1) (**e,j,o**), the overlay of all markers (**f,k,p**) and the enlarged view of the edge of the Lewy pathology in **f,n** and the LN in **p** (**g,l,q**). Images are representative across 14 PD donors for Lewy pathological inclusions with an outer layer of p-αSyn. Scale bars: **f,k,p**, 5 μm; **g,l,q**, 1μm.

method to provide visualization of filaments if these have a diameter of at least 5 nm and a length of at least 25 nm. Shorter or thinner filaments, or those bound to the observed membrane patches or to their edges, as well as smaller aggregates of αSyn including those potentially dissolved within lipidic membranes, might not be detectable in such electron microscopy images. For this reason, the high-resolution electron microscopy imaging approach employed here may under-report the amount of filaments that could be present in the LB/LN. Furthermore, it is important to note that clarifying the nature of the observed filaments in αSyn-immunopositive inclusions (that is, distinguishing abundant cytoskeletal filaments from αSyn filaments) was not possible in this study. For example, αSyn filaments in brain tissue are reported as similar in diameter (measuring between 5–12 nm) to neurofilaments (10 nm)[3,9]. Immunogold or related staining procedures for immuno-electron microscopy on postmortem brain tissues can provide sufficient resolution to localize filaments using immunogold markers[3]. However, clarifying whether immunogold localizes truly to filaments or to the aggregated (proteinaceous) material surrounding filaments in brain tissue extracts, can be challenging[9,18].

The protocols commonly used for tissue processing for electron microscopy preclude making reliable conclusions regarding immunopositive αSyn clusters with respect to the presence and identity of filaments versus actual αSyn filaments within Lewy pathology. This issue is further complicated when considering that mono- and multimeric forms of αSyn might simultaneously be present in this crowded intracellular environment[19], and that immunolabeling for αSyn tends to lack specificity for filaments. A further complicating factor is the filament extraction process itself that is based on protocols optimized for the extraction of paired helical and straight filaments of Alzheimer's diseased brains[9]. When such protocols were applied to DLB brains with concomitant tau and Aβ pathology[20,21], Aβ or tau filaments could not be distinguished from αSyn filaments.

While previous studies also indicated lipid content in LB in situ or as potential membranous contamination in brain extracts considered to contain LB[20], our discovery of a crowded environment of membrane fragments, mitochondria, vesicular structures, including some that resemble lysosomes and autophagosomes, intermingled with non-fibrillar αSyn in multiple pathological inclusions, provokes
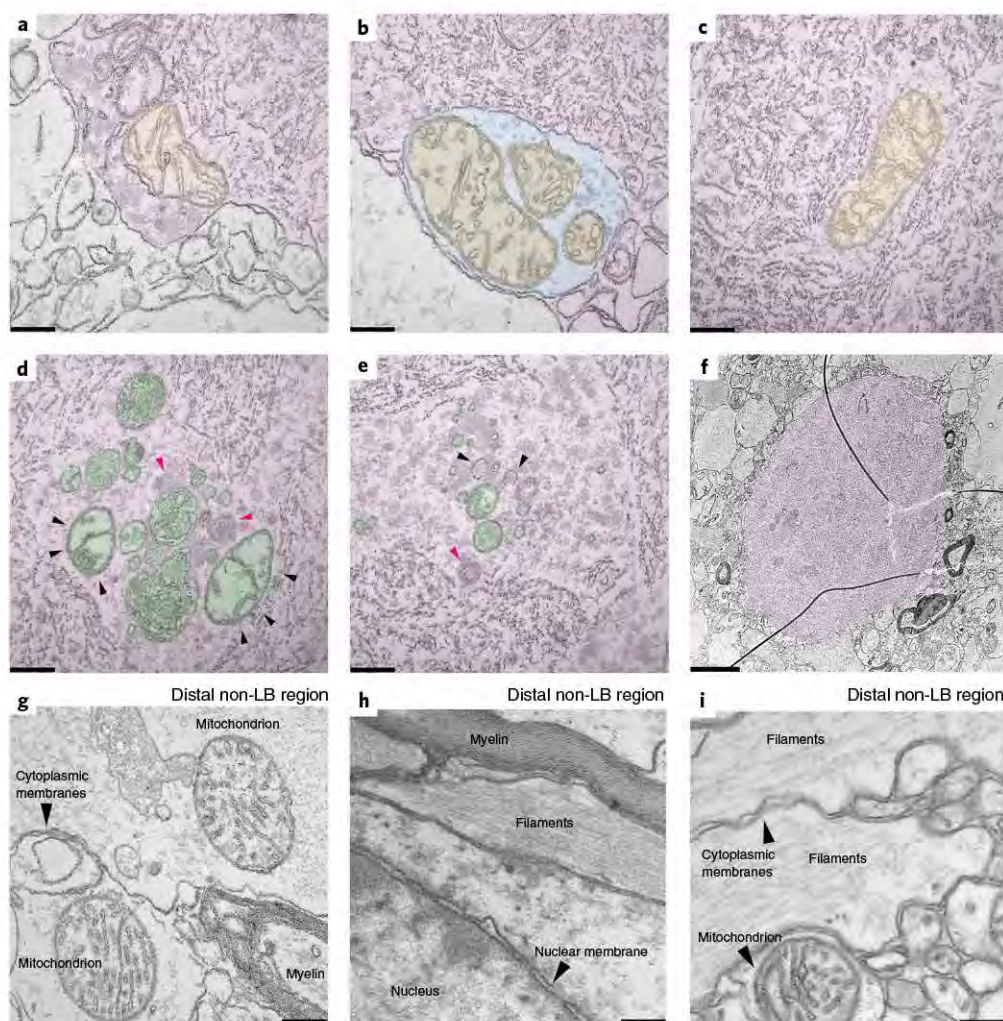
Fig. 8 | Inner architecture of Lewy pathology shows membrane fragments and organelles. Correlative TEM images of sections (50 nm thick) of an aggregate localized by SBFSEM in the SN of Donor B-PD. Images are artificially colored: overall inclusion, pink; membrane compartments, blue; mitochondria, orange; other organelles, green. **a**, Edge of the inclusion with a mitochondrion present. **b**, Another edge of the inclusion with mitochondria enclosed in a membrane-delimited compartment. **c**, Mitochondrion surrounded by membrane fragments within the inclusion. **d**, Putative mitochondria (black arrowheads) and lysosomes (pink arrowheads) within the inclusion. **e**, Membrane-bound structures resembling omegasomes (black arrowheads) and a lysosome (pink arrowhead), surrounded by fuzzy structures resembling proteinacious deposits within the inclusion. **f**, Overview of the Lewy pathological inclusion within the tissue. **g**, Two normal mitochondria with clear cristae in an area within the same tissue section but distal to the region with the inclusion. Cytoplasmic membranes and a myelin sheath are also present. **h**, Condensed filaments and myelin, along with nuclear membrane, in an area within the same tissue section but distal to the region with the inclusion. **i**, Typical cytoskeletal filaments, along with mitochondrion showing clear cristae, in an area within the same tissue section but distal to the region with the inclusion. Scale bars: **a**, 1.5 μm; all others, 200 nm.

new theories about the mechanisms contributing to the formation of Lewy pathology in PD. A recent study by Grassi and colleagues[22] has shown that non-fibrillar αSyn species produced from a partial autophagosomal digest appear to disrupt mitochondria in both post-mortem brain tissue and cell culture, corroborating our CLEM data (Figs. 1–3, 6b–d and 7a,b and Supplementary Fig. 6). Although the impact on mitochondrial maintenance for specific genes mutated in idiopathic PD (except for *SNCA*) is difficult to specify[23], our findings of mitochondria around and within LB, many of which appear distorted and clustered together or in a damaged state, indicate potential mitochondrial instability or dysfunction in disease-affected neurons. Mitochondrial homeostasis is known to be influenced by αSyn, which interacts with mitochondria-associated endoplasmic reticulum membranes, and is suggested to play a role in disrupting autophagy, endosomal transport and endoplasmic reticulum traffic to the Golgi[24]. Furthermore, the recently described new pathogenic

variant in *LRP-10* described in Donor B-PD has been linked to disturbance of intracellular membrane trafficking in PD[25].

The crowded multitude of organelles we observe may also represent a result of the cell's efforts to sequester problematic lipid-based contents associated with αSyn into an aggresome-like structure. McNaught and colleagues have shown that LB are immunoreactive for several markers of aggresomes[26], deposits that form in response to cytoplasmic accumulation of misfolded proteins[27,28]. The formation of such LB may hence arise from an aggresome-like process[26,28]. Furthermore, studies have shown that crowding of αSyn on membranes not only changes the morphology of vesicles and mitochondria, but can also catalyze the formation of αSyn filaments[29], which may explain the presence of distorted mitochondria and vesicles in the LB analyzed in our work.

Our correlative TEM tomograms show that LN are also primarily composed of membrane fragments, dysmorphic mitochondria

and structures reminiscent of lysosomes and autophagosomes, as well as cytoskeletal building blocks. To our knowledge, this has not been reported before. The cytoskeletal abnormalities we recorded in LN by CLEM support the idea that neurofilaments become disrupted, possibly through proximally experiencing an increase of oxidative stress[30]. The 3D STED data also showed that LN contain many mitochondria and lysosomes. One could speculate that a crowded multitude of damaged organelles and proteins would be sufficient to disrupt axonal trafficking.

The precise form and location of αSyn within the LB and LN here observed by CLEM is not known. Since all Lewy pathology studied here were identified by their high content of αSyn, but primarily contained membranous material, αSyn must be present in these LB and LN in an alternate form besides filamentous; αSyn has been shown to be structurally polymorphic[31]. One possible interpretation is that αSyn may be acting as membrane tether[32], bridging different mitochondrial membrane patches and leading to excessive adhesion between mitochondrial membranes, which could have led to mitochondrial damage, membrane disruption and formation of Lewy pathology—consisting of fragmented organellar membranes, each excessively decorated with αSyn. Alternatively, αSyn might have disrupted the membrane integrity, leading to fragmented organelles, which subsequently clustered into LB. Either way, our data indicate that αSyn may modulate the compartmentalization and function of membranes and organelles in LB-affected cells, prompting a new hypothesis about the role of αSyn in the formation of Lewy pathology in PD (Supplementary Fig. 15).

The physiological role of αSyn in the presynaptic terminal includes remodeling of membranes, clustering of synaptic vesicles and maintaining synaptic vesicle pools, promoting SNARE-complex assembly and modulating the release cycle of synaptic vesicles[33]. The formation of structures called 'nanodiscs' by αSyn and lipids in vitro[34] has been reported. Our findings of membrane-rich Lewy pathology in human brain are similar to observations by electron microscopy in a transgenic mouse model that overexpresses human αSyn[35]. Boassa and colleagues reported alterations and enlargements of the presynaptic endomembrane systems in these mice, with presynaptic terminals filled with membrane-bound organelles, including tubulovesicular structures. Our findings of abundant membranes in human Lewy pathology support their animal model. Another study in rats demonstrated that αSyn interacts with tubulovesicular/vesicular structures, reminiscent of those visualized by our CLEM, through its amino-terminal repeat region[36]. Furthermore, a recent in vitro study shows a clustering of mitochondria and other membranous structures in the neuronal cell body when seeded with recombinant αSyn filaments[37]. In future experiments, it will be interesting to explore how αSyn influences the formation of Lewy pathology in concert with vesicles and cytoplasmic organelles. It is also relevant to explore whether the animal and cellular models of intracellular αSyn accumulation reveal similarities to our observation in human brain, thereby leading to more representative translational models of PD and related synucleinopathies.

Our work provides a new dimension of understanding of Lewy pathology in the human brain, with nanoscale imaging that is cross-validated by orthogonal biophysical methods. We present here a new theoretical model in which lipid membrane fragments and distorted organelles together with a non-fibrillar form of αSyn are the main structural building blocks for the formation of Lewy pathology (Supplementary Fig. 15). Our model for the formation of these highly membranous αSyn-immunopositive inclusions is supported by evidence from existing studies that demonstrate αSyn as capable of disrupting mitochondrial membranes, manipulating and organizing membrane components, and inducing membrane curvature to vesicles under certain conditions[22,38–41].

Together, our results support the hypothesis of impaired organellar trafficking as a potential driver of pathogenesis in PD. Further studies are now required to study the morphology of Lewy pathology across different Braak stages of PD, and to analyze the brain tissue ultrastructure in related synucleinopathies. Our findings emphasize the need to consider population heterogeneity of Lewy pathology and that lipids are a major component of them. This has strong implications for the understanding of the pathogenesis of PD. It could lead to new approaches for cellular and in vivo models, support the rationale for the development of biomarkers such as positron emission tomography tracers for Lewy pathology, and point to new drug targets for Parkinson's and related diseases.

Online content
Any methods, additional references, Nature Research reporting summaries, source data, statements of code and data availability and associated accession codes are available at https://doi.org/10.1038/s41593-019-0423-2.

References
1. Goedert, M., Spillantini, M. G., Del Tredici, K. & Braak, H. 100 years of Lewy pathology. *Nat. Rev. Neurol.* **9**, 13–24 (2013).
2. Wakabayashi, K. et al. The Lewy body in Parkinson's disease and related neurodegenerative disorders. *Mol. Neurobiol.* **47**, 495–508 (2013).
3. Arima, K. et al. Immunoelectron-microscopic demonstration of NACP/alpha-synuclein-epitopes on the filamentous component of Lewy bodies in Parkinson's disease and in dementia with Lewy bodies. *Brain Res.* **808**, 93–100 (1998).
4. Klein, C. & Schlossmacher, M. G. Parkinson disease, 10 years after its genetic revolution: multiple clues to a complex disorder. *Neurology* **69**, 2093–2104 (2007).
5. Spillantini, M. G. et al. Alpha-synuclein in Lewy bodies. *Nature* **388**, 839–840 (1997).
6. Braak, H., Sandmann-Keil, D., Gai, W. & Braak, E. Extensive axonal Lewy neurites in Parkinson's disease: a novel pathological feature revealed by alpha-synuclein immunocytochemistry. *Neurosci. Lett.* **265**, 67–69 (1999).
7. Braak, H., Ghebremedhin, E., Rub, U., Bratzke, H. & Del Tredici, K. Stages in the development of Parkinson's disease-related pathology. *Cell Tissue Res.* **318**, 121–134 (2004).
8. Goedert, M. Neurodegeneration. Alzheimer's and Parkinson's diseases: the prion concept in relation to assembled Abeta, tau, and alpha-synuclein. *Science* **349**, 1255555 (2015).
9. Spillantini, M. G., Crowther, R. A., Jakes, R., Hasegawa, M. & Goedert, M. Alpha-synuclein in filamentous inclusions of Lewy bodies from Parkinson's disease and dementia with Lewy bodies. *Proc. Natl Acad. Sci. USA* **95**, 6469–6473 (1998).
10. Forno, L. S. Neuropathology of Parkinson's disease. *J. Neuropathol. Exp. Neurol.* **55**, 259–272 (1996).
11. Hunn, B. H., Cragg, S. J., Bolam, J. P., Spillantini, M. G. & Wade-Martins, R. Impaired intracellular trafficking defines early Parkinson's disease. *Trends Neurosci.* **38**, 178–188 (2015).
12. Morell, P. & Quarles, R. H. in *Basic Neurochemistry: Molecular, Cellular and Medical Aspects* 6th edn (eds Siegel G. J. et al.) Chapter 4 (Lippincott-Raven, 1999).
13. Nixon, R. A. Autophagy, amyloidogenesis and Alzheimer disease. *J. Cell Sci.* **120**, 4081–4091 (2007).
14. Eichmann, C. et al. Preparation and characterization of stable alpha-synuclein lipoprotein particles. *J. Biol. Chem.* **291**, 8516–8527 (2016).
15. Liu, Y. L. et al. Alternation of neurofilaments in immune-mediated injury of spinal cord motor neurons. *Spinal Cord.* **47**, 166–170 (2009).
16. Navarro, P. P. et al. Cerebral corpora amylacea are dense membranous labyrinths containing structurally preserved cell organelles. *Sci. Rep.* **8**, 18046 (2018).
17. Kuusisto, E., Parkkinen, L. & Alafuzoff, I. Morphogenesis of Lewy bodies: dissimilar incorporation of alpha-synuclein, ubiquitin, and p62. *J. Neuropathol. Exp. Neurol.* **62**, 1241–1253 (2003).
18. Spillantini, M. G. Parkinson's disease, dementia with Lewy bodies and multiple system atrophy are alpha-synucleinopathies. *Parkinsonism Relat. Disord.* **5**, 157–162 (1999).
19. Peng, C. et al. Cellular milieu imparts distinct pathological alpha-synuclein strains in alpha-synucleinopathies. *Nature* **557**, 558–563 (2018).
20. Iwatsubo, T. et al. Purification and characterization of Lewy bodies from the brains of patients with diffuse Lewy body disease. *Am. J. Path.* **148**, 1517 (1996).

21. Jellinger, K. A. & Korczyn, A. D. Are dementia with Lewy bodies and Parkinson's disease dementia the same disease? *BMC Med.* **16**, 34 (2018).
22. Grassi, D. et al. Identification of a highly neurotoxic alpha-synuclein species inducing mitochondrial damage and mitophagy in Parkinson's disease. *Proc. Natl Acad. Sci. USA* **115**, E2634–E2643 (2018).
23. Ryan, B. J., Hoek, S., Fon, E. A. & Wade-Martins, R. Mitochondrial dysfunction and mitophagy in Parkinson's: from familial to sporadic disease. *Trends Biochem .Sci.* **40**, 200–210 (2015).
24. Wong, Y. C. & Krainc, D. alpha-synuclein toxicity in neurodegeneration: mechanism and therapeutic strategies. *Nat. Med.* **23**, 1–13 (2017).
25. Quadri, M. et al. LRP10 genetic variants in familial Parkinson's disease and dementia with Lewy bodies: a genome-wide linkage and sequencing study. *Lancet Neurol.* **17**, 597–608 (2018).
26. McNaught, K. S., Shashidharan, P., Perl, D. P., Jenner, P. & Olanow, C. W. Aggresome-related biogenesis of Lewy bodies. *Eur. J. Neurosci.* **16**, 2136–2148 (2002).
27. Johnston, J. A., Ward, C. L. & Kopito, R. R. Aggresomes: a cellular response to misfolded proteins. *J. Cell Biol.* **143**, 1883–1898 (1998).
28. Olanow, C. W., Perl, D. P., DeMartino, G. N. & McNaught, K. S. Lewy-body formation is an aggresome-related process: a hypothesis. *Lancet Neurol.* **3**, 496–503 (2004).
29. Viennet, T. et al. Structural insights from lipid-bilayer nanodiscs link α-Synuclein membrane-binding modes to amyloid fibril formation. *Comm. Biol.* **1**, 44 (2018).
30. Giasson, B. I. et al. Oxidative damage linked to neurodegeneration by selective alpha-synuclein nitration in synucleinopathy lesions. *Science* **290**, 985–989 (2000).
31. Nugent, E., Kaminski, C. F. & Kaminski Schierle, G. S. Super-resolution imaging of alpha-synuclein polymorphisms and their potential role in neurodegeneration. *Integr. Biol. (Camb.)* **9**, 206–210 (2017).
32. Fusco, G. et al. Structural basis of synaptic vesicle assembly promoted by alpha-synuclein. *Nat. Commun.* **7**, 12563 (2016).
33. Burre, J. The Synaptic function of alpha-synuclein. *J. Park. Dis.* **5**, 699–713 (2015).
34. Mizuno, N. et al. Remodeling of lipid vesicles into cylindrical micelles by alpha-synuclein in an extended alpha-helical conformation. *J. Biol. Chem.* **287**, 29301–29311 (2012).
35. Boassa, D. et al. Mapping the subcellular distribution of alpha-synuclein in neurons using genetically encoded probes for correlated light and electron microscopy: implications for Parkinson's disease pathogenesis. *J. Neurosci.* **33**, 2605–2615 (2013).
36. Jensen, P. H., Nielsen, M. S., Jakes, R., Dotti, C. G. & Goedert, M. Binding of alpha-synuclein to brain vesicles is abolished by familial Parkinson's disease mutation. *J. Biol. Chem.* **273**, 26292–26294 (1998).
37. Mahul-Mellier, A.-L. et al. The making of a Lewy body: the role of α-synuclein post-fibrillization modifications in regulating the formation and the maturation of pathological inclusions. Preprint at *bioRxiv* https://doi.org/10.1101/500058 (2018).
38. Shi, Z., Sachs, J. N., Rhoades, E. & Baumgart, T. Biophysics of alpha-synuclein induced membrane remodelling. *Phys. Chem. Chem. Phys.* **17**, 15561–15568 (2015).
39. Jiang, Z., de Messieres, M. & Lee, J. C. Membrane remodeling by alpha-synuclein and effects on amyloid formation. *J. Am. Chem. Soc.* **135**, 15970–15973 (2013).
40. Westphal, C. H. & Chandra, S. S. Monomeric synucleins generate membrane curvature. *J. Biol. Chem.* **288**, 1829–1840 (2013).
41. Nuber, S. et al. Abrogating native α-synuclein tetramers in Mice causes a L-DOPA-responsive motor syndrome closely resembling Parkinson's disease. *Neuron* **100**, 75–90 (2018). e75.

Author contributions

S.H.S. performed CLEM/TEM and tomography, SBFSEM imaging and 2D/3D color segmentations, analyzed data and wrote the manuscript. A.J.L. performed CLEM/TEM and tomography, and contributed to analyzing the data and writing the manuscript. C.G. and A.G.M. trained and supported S.H.S. and A.J.L. with SBFSEM and CLEM tissue preparation and imaging. J. Hench screened light microscopy slides and analyzed light microscopy data of CLEM for localizing Lewy pathology. J. Hench, G.S. and A.J.L. designed and optimized the staining for CLEM and localization of Lewy pathology in light microscopy data with S.H.S. W.D.J.v.d.B., T.M. and E.H. performed STED imaging. P.P.N. trained and supported A.J.L. in sample preparation, data collection and image processing for TEM tomography. K.N.G. and J.W. assisted with TEM tomography. R.S. and S.H.S. optimized and performed lipid and αSyn co-staining and confocal imaging. D.C.-D. performed subtomogram analysis. A.I. processed tissue samples collected at the autopsy room, prepared cryostat tissue and sectioned paraffin embedded tissue. Y.d.G. prepared cryostat tissue for CARS and FTIR imaging. A.J.M.R. and W.D.J.v.d.B. performed rapid autopsies of PD brain donors and controls, collected brain tissue and preformed neuropathological assessment. W.D.J.v.d.B. performed neuroanatomical dissections and performed laser-capture micro dissection with S.H.S. A.D.P. performed Raman imaging tests. J.E., A.S. and J. Hoernschemeyer performed LC–MS analysis. D.N., S.F.E.M. and K.N.G. performed and analyzed CARS imaging. F.G. performed FTIR imaging. M.Q., W.F.J.v.I.J. and V.B. provided whole exome sequencing and genetic analysis of PD brain donors. B.B. provided technical input to electron microscopy analysis of brain tissue in neurodegeneration. S.F. provided expertise in neuropathology, differentiation of Lewy pathology versus corpora amylacea, and provided optical microscopy data of corpora amylacea and Lewy pathology in same tissues. M.B., H.S., W.D.J.v.d.B. and M.E.L. designed research, analyzed and interpreted the data, and contributed to writing the manuscript.

Competing interests

A.d.P., J.E., A.S., J. Hoernschemeyer, B.B., M.B. and M.E.L. are full-time employees of Roche/F. Hoffmann–La Roche Ltd, and they may additionally hold Roche stock and/or stock options.

Additional information

Supplementary information is available for this paper at https://doi.org/10.1038/s41593-019-0423-2.

Reprints and permissions information is available at www.nature.com/reprints.

Correspondence and requests for materials should be addressed to H.S., W.D.J.V.B. or M.E.L.

Peer review information: *Nature Neuroscience* thanks Tim Bartels, Roxana Carare, Robert Edwards and the other, anonymous, reviewer(s) for their contribution to the peer review of this work.

Publisher's note: Springer Nature remains neutral with regard to jurisdictional claims in published maps and institutional affiliations.

Methods

Human postmortem brain tissue samples. Postmortem tissue samples for electron microscopy and STED studies from five donors (Donors A–E) with clinical diagnosis PD with dementia (PDD) and one non-neurological control (Donor F-Control), as well as postmortem tissue samples for STED studies from nine donors (Donors G–O) with clinical diagnosis PDD, all with ~5 h postmortem delay, were obtained from the Netherlands Brain Bank (NBB, www.brainbank.nl) and the Normal Aging Brain Collection (Department of Anatomy and Neurosciences, VUmc), respectively (Supplementary Table 1). Tissues were collected using a rapid autopsy protocol (NBB). All donors had given written informed consent for a brain autopsy and the use of the material and clinical information for research purposes. Detailed neuropathological and clinical information was made available, in compliance with local ethical and legal guidelines, and all protocols were approved by the local institutional review board.

At autopsy, four 0.5-cm-thick adjacent brain slices of the mesencephalon and hippocampus (mid) were collected. Cubes of ~1–2 mm³ of the ventral part of the substantia nigra pars compacta (SNpc) and hippocampal CA2 regions were dissected and fixed for 6 h in a mixture of 2% paraformaldehyde/2.5% glutaraldehyde in 0.15 M cacodylate buffer with 2 mM calcium chloride, pH 7.4 and then washed with PBS. One slice of mesencephalon and hippocampus was directly snap-frozen for processing for LCM and subsequent lipidomics and CARS analysis.

The PD brain donors fulfilled the United Kingdom Parkinson's Disease Society Brain Bank (UK-PDSBB) clinical diagnostic criteria for PD[42]. Neuropathological evaluation was performed on 7 μm formalin-fixed paraffin-embedded sections collected from multiple brain regions according to the guidelines of BrainNet Europe. As is routine for such brain donors, staging of Alzheimer's disease was evaluated according to the Braak criteria for NFTs[43], Consortium to Establish a Registry for Alzheimer's Disease (CERAD) criteria adjusted for age and Thal criteria[44]. The presence and topographical distribution of αSyn (monoclonal mouse anti-human-α-synuclein, clone KM51, Monosan; see Supplementary Fig. 1) was rated according to Braak's staging scheme for αSyn[7] and a modified version of McKeith's staging system for αSyn (that is, brainstem, limbic system, amygdala-predominant or neocortical[45]).

Disease staging. Staging of LB disease and Alzheimer's disease related pathology was performed based on Brain Net Europe consensus guidelines (αSyn[46], NFT[47], amyloid-β[48]) and National Institute on Aging-Alzheimer's Association criteria[49]. Additionally, brain tissue was also inspected for other salient pathology such as age-related tau astrogliopathy[50], cerebral white matter rarefactions, cerebral amyloid angiopathy[51] and (micro)infarctions and hemorrhages and TAR DNA-binding protein pathology[52].

Whole exome sequencing and PD gene analysis. Postmortem brain tissues from donors used for these electron microscopy studies (Supplementary Table 1) were analyzed by whole exome sequencing with a focus on the analysis of the PARK genes and additionally some genetic risk factors for dementia. No listed known causative genetic variants were detected in the donors. In Donor B-PD, a variant was detected in the *LRP-10* gene, a potential new gene causal for PD that needs yet to be confirmed by others, as previously described[25]. Variants were to be reported if they fulfilled the following four criteria: (1) variant(s) located within the following list of genes associated with PD or Parkinsonian syndromes: *ATP13A2, ATP6AP2, CHCHD2, DNAJC13, DNAJC6, EIF4G1, FBXO7, GBA, LRRK2, PARK2, PARK7, PINK1, PLA2G6, RAB39B, SNCA, SYNJ1, TARDBP, VPS35, VPS13C, MAPT, GRN, TMEM230, POLG, DCTN1* and *PTRHD1*; (2) possible splicing variants→intronic or exonic variants located within 10 base pairs at the exon-intron boundaries; (3) exonic variants that have a coding effect (synonymous variants have been excluded); and (4) new variants or variants present with a minor allele frequency (below 1%) in the following publicly available databases: NHLBI Grand Opportunity Exome Sequencing Project (http://evs.gs.washington.edu/EVS/); Exome Aggregation Consortium Browser (http://exac.broadinstitute.org/); 1,000 Genomes (http://browser.1000genomes.org/index.html); dbSNPs (https://www.ncbi.nlm.nih.gov/projects/SNP/) and Genome of the Netherlands (GoNL) (http://www.nlgenome.nl/).

CLEM. The CLEM[53] workflow is summarized in Supplementary Fig. 4, and pictorially shown in Supplementary Figs. 2 and 3. Fixed postmortem human brain tissue (2% filtered paraformaldehyde/2.5% glutaraldehyde in 0.15 M cacodylate buffer with 2 mM calcium chloride, pH 7.4) was washed in cacodylate buffer and kept at 4 °C for 1–2 d. Tissue sections were then collected at 40–60 μm on a vibratome and washed in cold cacodylate buffer, post-fixed in potassium ferrocyanide in cacodylate buffer with osmium tetroxide, washed with double-distilled water and immersed in filtered thiocarbohydrazide solution. After this second wash step, sections were post-fixed in osmium tetroxide, rinsed again and stained with uranyl acetate at 4 °C overnight. The following day, sections were rinsed, stained with lead aspartate solution at 60 °C, dehydrated in a graded alcohol series on ice, and embedded in Durcupan resin. After resin hardening, small pieces of the resin-embedded tissue (~1 × 1 mm) were cut and mounted on standard aluminum pins, then physically cut using a razor blade into a trapezoid shape, which is optimal for the collection of serial tissue sections.

All tissues sections were generated using a physical ultramicrotome (Ultracut EM UC7, Leica Microsystems) and cut at a thickness of 100–200 nm. They were alternately collected on Superfrost Plus glass slides (Thermo Fisher Scientific) for later light microscopy and electron microscopy grids (EMS Diasum) with a carbon-stabilized formvar film for TEM imaging. Slides were processed for immunohistochemistry using mouse anti-αSyn (Invitrogen 180215, LB509 concentrate) diluted 1:500. The sections were etched in a saturated ethanolic potassium hydroxide solution for 5 min followed by washing in PBS. Endogenous peroxidases were quenched with 1% hydrogen peroxide in 10% methanol for 10 min followed by blocking in antibody diluent (Dako/S202230) for 10 min. The sections were incubated in primary antibody for 1 h at 37 °C followed by washing with 0.25% Triton X-100 in PBS and incubation with the Immpress Reagent Anti-Mouse Ig (Vector/VC-MP-7401) secondary antibody for 30 min at room temperature. Bound antibody complexes were detected using the Permanent HRP Green Kit (Zytomed Systems) with incubation for 3 min at room temperature, before counterstaining with hematoxylin, dehydration and coverslipping.

The slides were screened by light microscopy and compared side by side to identify Lewy pathology. Light microscopy images of selected slides displaying αSyn-immunopositive inclusions were collected at ×40 magnification using a Zeiss Axiophot (Carl Zeiss Microscopy) with monochromatic light, or at ×60 magnification using a Nikon Ti-E widefield and the images were manually stitched together using Adobe Photoshop CS6 (Adobe Systems) or FIJI[54] to create a montage revealing the trapezoid shape of an individual tissue section. The full montage representing the individual tissue section was then cropped to the limits of the tissue borders using an edge-detection lasso tool, which followed the trapezoid shape of the tissue sections. TEM images of electron microscopy grids that contained tissue sections immediately adjacent to those on the selected light microscopy slides, were collected either on a Talos 200keV TEM (FEI, Thermo Fisher Scientific) and manually stitched together using Adobe Photoshop, or on a Titan Krios 300keV TEM (FEI, Thermo Fisher Scientific) using the SerialEM[55] montage option. The resulting electron microscopy montage was overlaid with the corresponding light microscopy montage obtained for the alternating tissue sections collected on a glass slide, to define the specific location of the αSyn-immunopositive inclusions in the TEM images (Supplementary Figs. 2–5) and guide the collection of subsequent higher resolution images and electron tomography. The collection of serial tissue sections on a single electron microscopy grid meant that the same αSyn-immunopositive inclusion was present multiple times and that obstruction of the inclusion by a grid bar was not an issue, since another section of the same grid, where it was not obscured, could be used.

For TEM tomography, samples were imaged at cryogenic temperatures using a Titan Krios (FEI, Thermo Fisher Scientific) equipped with a Quantum-LS energy filter (20 eV slit width) and a K2 Summit direct electron detector (Gatan) and operated at 300 kV acceleration voltage, or at room temperature on a Talos (FEI, Thermo Fisher Scientific) operated at 200 kV. Tilt series were recorded using the SerialEM software[55] with a unidirectional tilt-scheme at 2–3° increments or a 'dose-symmetric Hagen tilt-scheme'. The latter procedure begins at low tilt and then alternates between increasingly positive and negative tilts to maximize the amount of high-resolution information maintained in the tomogram for subsequent subtomogram averaging and 3D color segmentation, and also yields improved tracking between sequential tilt angles[56]. Images for the tilt series were collected at 3° increments over a range between −60° and 60° at a nominal defocus within a range of 6–10 μm.

Tilt series alignment by cross-correlation and patch-tracking followed by 3D reconstruction of unbinned tomograms were performed using *etomo* of the IMOD software[57]. Resulting tomograms were reduced by a factor of two in all dimensions. Semi-automatic 3D color segmentation of the tomograms was performed by user-interactive thresholding and volume rendering using the Amira 6.0 software (FEI, Thermo Fisher Scientific). Videos of 3D color-segmented tomograms were created using Amira 6.0. Videos of reconstructed, non-color-segmented tomograms were created using IMOD software. Subtomographic texture analysis was carried out using the Dynamo software[58,59].

SBFSEM and CTEM. Fixed postmortem human brain tissue (2% filtered paraformaldehyde/2.5% glutaraldehyde in 0.15 M cacodylate buffer with 2 mM calcium chloride, pH 7.4) was washed in cacodylate buffer and kept at 4 °C for 1–2 d. Tissue sections were then collected at 40–60 μm on a vibratome, washed in cold cacodylate buffer, post-fixed in potassium ferrocyanide in cacodylate buffer with osmium tetroxide, washed with double-distilled water and immersed in filtered thiocarbohydrazide solution. After this step, sections were post-fixed in osmium tetroxide, rinsed again and stained with uranyl acetate at 4 °C overnight. The following day, sections were rinsed, stained with lead aspartate solution at 60 °C, dehydrated in a graded alcohol series on ice and embedded in Durcupan resin. After resin hardening, small pieces of the resin-embedded tissue (~ 1 × 1 mm) were cut and mounted on standard aluminum pins. The samples on the pins were sputter-coated with gold and platinum in a vacuum system (Quorum) to enhance sample conductivity for SEM imaging, and then directly transferred to the SEM chamber for imaging.

Data were collected using a serial block-face scanning electron microscope (FEI Quanta200FEG, Thermo Fisher Scientific) equipped with a physical

microtome (3View, Gatan) inside the microscope observation chamber[60]. An accelerating voltage of 3.5 keV, a spot size of three, a scanning speed of 2 μs per pixel and the high vacuum mode were used. After each iterative removal of an ultrathin slice (70 nm thick) by a diamond knife within the SEM chamber, the surface of the remaining block (specimen) was imaged. Images with 8,192 × 8,192 or 4,096 × 4,096 pixels were collected at 7–10 nm per pixel along both the x and y axes using the Digital Micrograph software (Gatan). Image series of regions of interest were further processed, digitally aligned and reconstructed into 3D z-stacks or tomograms using the TrakEM2 module of FIJI (https://fiji.sc).

To enable correlative TEM, once a region of interest containing inclusion bodies was identified and partly imaged by SEM, the sample was removed from the SEM chamber and cut using a physical ultramicrotome (Ultracut EM UC7, Leica Microsystems). The resulting 30–50 nm-thick slices obtained were sequentially collected on electron microscopy grids (EMS Diasum) with a carbon-stabilized formvar film, and imaged at room temperature using a Philips CM10 electron microscope operated at 80 kV. Electron micrographs were recorded on a 2,048 × 2,048-pixel charge-coupled device camera (Veleta, EMSIS). Color annotation of the resulting 2D micrographs was performed manually using Adobe Photoshop CS6 (Adobe Systems).

Lipid–αSyn co-staining and fluorescence imaging. Tissue sections (10 μm thick) of a snap-frozen tissue slice of the hippocampus (including CA2) of Donor A-PD and the SN of Donor B-PD were cut using a cryostat (Leica) collected on glass slides at −18 °C, shipped on dry ice from the VUmc to C-CINA, and subsequently stored at −80 °C. Immediately after removal from −80 °C, slides were fixed with 4% paraformaldehyde for 30 min in a humidity chamber. They were then rinsed in PBS and treated with 0.5% Triton X-100 in PBS, washed with PBS and incubated for 2 h at room temperature with a primary antibody to αSyn, LB509 (amino acid 115–122, abcam ab27766). After washing with PBS, slides were incubated for 1.5 h at room temperature with a cocktail of secondary fluorescence-conjugated antibody Alexa488 and DAPI (4′,6-diaidino-2-phenylindole, dilactate; BioLegend) to visualize nuclei. Slides were washed with PBS, and then treated with Nile Red stain (Sigma 19123) for 10 min in the dark. Nile Red powder was originally diluted to 0.5 mg ml⁻¹ in acetone to make a stock solution, and a fresh working solution was prepared every time by diluting an aliquot of this stock 1:200-fold in 75% glycerol. Stained slides were washed in 75% glycerol, treated with Sudan Black in the dark, rinsed in PBS and mounted in Mowiol coverslip mounting solution. They were allowed to dry in the dark overnight, and then stored at 4 °C in the dark before imaging.

Confocal fluorescence images (1,024 × 1,024 pixels) were mainly acquired at a magnification of ×40, using a point-scanning confocal microscope (CLSM Leica TCS SPE with a DMI4000 microscope) equipped with advanced correction system objectives and the solid-state laser system: 405 nm (DAPI), 488 nm (Alexa488) and 635 nm (Nile Red). Composite images and co-localizations were calculated and created using standard tools in the Imaris software (Oxford Instruments) and final figures were composed in Adobe Photoshop CS6 (Adobe Systems). Untreated tissue samples were checked by light microscopy before and after staining/labeling to look for auto-fluorescence, as this could interfere with label detection and then by CLSM to visualize greater detail in two and three dimensions. As a further control, tissue sections were treated with the secondary fluorescence antibody alone, without the primary antibody and examined by light microscopy and CLSM to check for unspecific labeling.

Co-labeling for STED microscopy. Multiple labeling experiments were performed on formalin-fixed, paraffin-embedded 20-μm-thick midbrain and hippocampus sections, using markers for organelles and αSyn. For heat-induced antigen retrieval, sections were placed in sodium citrate buffer (pH 6.0) in a steamer at 90–99 °C for 30 min. Antibodies against VDAC1/Porin (Abcam ab14734), LAMP-1 (Abcam ab24170) and S129-phosphorylated α-synuclein (pSer129 Ab 11A5) directly labeled with AlexaFluor 488 were used. Abberior STAR 580 and STAR 635P fluorophores (Abberior, Bioconnect) were used as secondary antibodies. Nuclei were visualized by DAPI staining (Sigma).

STED microscopy was performed on a Leica TCS SP8 STED ×3 microscope (Leica Microsystems). Sections were irradiated with a pulsed white light laser at wavelengths of 499, 587 and 633 nm. A pulsed STED laser line at a wavelength of 775 nm was used to deplete the Abberior fluorophores (580, 635P), and a continuous wave STED laser with a wavelength of 592 nm was used to deplete the Alexa488 fluorophore. Further, to obtain confocal images of the DAPI signal, sections were irradiated with a solid-state laser at a wavelength of 405 nm. The DAPI signal was not depleted. All signals were detected using a gated hybrid detector in counting mode. Images were acquired using a HC PL APO CS2 ×100 1.4 numerical aperture oil objective lens, and the resolution was set to a pixel size of 20 × 20 nm. Finally, deconvolution was performed with Huygens Professional (Scientific Volume Imaging, Huygens). Images were adjusted for brightness/contrast in ImageJ (National Institute of Health), and final figures were composed using Adobe Photoshop CS6 (Adobe Systems).

LC–MS and lipidomics of microdissected tissues. Cryostat-cut tissue sections (7 μm) of the hippocampus (mid) of Donor A-PD, the mesencephalon of Donor

B-PD, and the corpus callosum of a non-neurological control donor (Donor F-Control) were collected at −18 °C. Sections were stained with hematoxylin (Sigma) for 1 min, washed under tap water for 5 min, quickly washed in sterile water, then stained with Eosin for 10 s. They were washed in 96% EtOH for 30 s, 100% EtOH for 30 s, then air-dried under a chemical fume hood before laser-capture microdissection (LCM). For the second LCM run, adjacent 7-μm-thick sections of the Donor A-PD hippocampus were immunostained with an antibody against αSyn FL-140 (sc-10717, Santa Cruz; dilution 1:2,000) for 30 min after fixation with 96% EtOH. After rinsing with PBS, the immunostaining was visualized with Envision detection systems peroxidase/DAB (DAKO). Sections were rinsed again with Tris-HCl (pH 7.4) and running tab water, subsequently air-dried and stored at 4 °C.

LCM was used to obtain approximately 3,000 αSyn-immunopositive inclusions from the CA2 of Donor A-PD and 2,700 LB from the SN of Donor B-PD. In both cases, these inclusions were laser-cut from inverted adjacent tissue polyethylene naphthalate membrane slides positioned on the stage of a LMD6500 (Leica Microsystems) microscope, collected in the cap of either 0.2 or 0.5 ml Eppendorf tubes, and kept on ice until further processing for mass spectrometry. Dentate gyrus region was also laser-cut from hippocampus of Donor A-PD as a additional control, and myelin-rich regions were laser-cut from the corpus callosum (myelin-rich, hence lipid-rich) of a non-neurological control brain donor.

For mass spectrometry, 40–60 μl of chloroform:methanol 2:1 (v/v) was carefully added to the inverted caps and shaken gently to dissolve the collected αSyn-immunopositive patches. The closed tubes were inspected using a magnification glass to ensure that there was no undissolved material. When this was the case, they were analyzed by LC–MS. A Dionex Ultimate 3000 RSLC nano-ultra performance liquid chromatography system with Reprospher 100 Si column (3 μm, 150 × 0.4 mm, 100 Å, Dr Maisch) was used to separate the isolated material by normal phase liquid chromatography. The column temperature was set to 40 °C with a flow rate of 10 μl min⁻¹. Mobile phase A was isopropanol:hexane:100 mM ammonium carboxylate 58:40:2 (v/v/v) and mobile phase B was isopropanol:hexane:100 mM ammonium carboxylate 50:40:10 (v/v/v)[61]. After an initial phase at 40% B for 5 min, the gradient was ramped up from 40 to 100% B over 25 min and followed by a steady phase at 100% B for 5 min.

To identify the eluting peaks, the capillary nano-ultra performance liquid chromatography was connected to a Waters Synapt G2 HRMS mass spectrometer. The mass signals and their fragments were obtained by a mass spectrometry scan and a survey tandem mass spectrometry scan method. A standard off/axis ESI source was used as an atmosphere-vacuum interface. The spray voltage was set to 2.8 kV, the desolvation temperature was set to 200 °C, and the source temperature was set to 100 °C. The tandem mass spectrometry spectra were obtained using mass-dependent collision energies. Waters Masslynx and Progeenesis QI software was used to evaluate the data.

Correlative CARS/FTIR and immunofluorescence imaging. Cryostat-cut tissue sections (10 μm) of the CA2 of Donor A-PD, SN of Donor B-PD and white matter of Donor F-Control were collected at −18 °C in the same manner as prepared for confocal immunofluorescence imaging, and dried under a stream of dry air at room temperature before CARS[62] or FTIR imaging. No stain was applied before imaging. Only data from Donor A-PD is shown (Supplementary Figs. 15 and 16).

CARS images were acquired using a commercial setup consisting of a picosecond-pulsed laser system that generates two synchronized beams collinearly aligned in an inverted confocal microscope (TCS SP5 II CARS; Leica Microsystems). In this setup, a fraction of the fundamental light of an Nd:YVO4 (HighQ Laser) at 1,064 nm is coupled into the microscope and used as a Stokes beam in the CARS process. The frequency-doubled output (532 nm) is used to synchronously pump an optical parametric oscillator (picoEmerald, APE), tunable in the 780–960 nm range. The laser beams are focused into the tissue by an HCX IRAPO L water immersion objective (×25/0.95W CORR, Leica Microsystems). The forward-detected CARS signal is measured via a non-descanned detector. The mean laser power was measured at the tissue position and found to be 28 and 21 mW at 816 and 1,064 nm, respectively. A typical pixel dwell time of 32 μs per scan was selected (31 s per image, 1,024 × 1,024 pixels covering up to 300 × 300 μm sample area, pixel resolution 300 nm[63]). CARS images of tissues were measured at 816 and 806 nm, which correspond to 2,850 cm (lipids, CH₂) and 2,930 cm (proteins, CH₃). The lipid and protein distribution profiles in αSyn-immunopositive inclusions were calculated using the Image Processing and Statistic toolboxes of MATLAB (The Mathworks, Inc.).

For the FTIR[64] measurements, infrared hyperspectral data acquisition was performed in transflection mode using an Agilent Cary 620 microscope with an Agilent Cary 670 spectrometer (Agilent). Spectral data were collected by a mercury cadmium telluride focal plane array detector with 128 × 128 elements, providing a field of view of approximately 422 × 422 μm with a ×25 magnification. The spectral data were collected from 3,700 to 950 cm⁻¹ with a spectral resolution of 4 cm⁻¹. Fourier transformation was performed with a Mertz phase correction, Blackman–Harris four-term apodization and a zero filling of two. A high numeric aperture of 0.82 was used[65]. Tissue sections were prepared on MirrIR low-e-slides (Kevley) for the transflection (reflection-absorption) measurements. The second derivative that minimizes the effects of the standing wave artifact was tested in addition. This

resulted in the same spectral band positions. Therefore, the vector-normalized spectra were used.

The resulting raw spectral maps were pre-processed using the previously described workflow[66]. Strong artifacts possibly arising from cracks or folds in the tissue were eliminated by quality control based on the signal-to-noise ratio and the integral of the amide I band. The remaining spectra were subjected to a Mie and resonance-Mie correction based on Extended Multiplicative Signal Correction, EMSC[67] in the wavenumber range from 3,100 to 950 cm^{-1}. The correction was performed with 30 iteration steps. Higher numbers of iteration steps (up to 100) were tested but the resulting spectra did not show further variances.

For immunofluorescence staining, after CARS or FTIR imaging tissue sections were kept on the slides and fixed with 4% formaldehyde for 30 min. Slides were rinsed and shipped in PBS, then treated with 0.5% Triton X-100 in PBS for 10 min. Slides were rinsed with PBS before incubation for 2 h at room temperature with an antibody targeting phosphorylated αSyn, phospho-S129 (pS129, abcam ab59264). After washing with PBS, sections were incubated for 1.5 h at room temperature with a secondary fluorescent antibody (Alexa488), rinsed again with PBS and applied with the next primary antibody to αSyn, LB509 for another 2 h at room temperature. After rinsing with PBS, sections were incubated for 1.5 h at room temperature with a secondary fluorescent antibody (Alexa647), rinsed in PBS, and applied with Sudan Black for 30 min. After rinsing again in PBS, they were finally mounted in Mowiol and allowed to dry in the dark overnight, subsequently being stored at 4 °C.

Brightfield and immunofluorescence images corresponding to each CA2 region imaged by CARS or FTIR were collected at ×10 magnification using a confocal microscope (Leica TCS SP5 CARS with a DMI3000). Images from brightfield/immunofluorescence and CARS or FTIR were overlaid and aligned to each other based on the morphology of tissue edges and lipofuscin deposits that appeared as black granules in the cell soma. Images were collected using an Ar-laser with 488 nm (Alexa488) excitation. An overlay of CARS or FTIR images with their counterparts showing αSyn immunofluorescence was performed using Adobe Photoshop CS6 (Adobe Systems).

Data blinding and randomization. Data collection and analysis were not performed blind to the conditions of the experiments. No data blinding or randomization was applied. The anonymized patient history had been known to the researchers before imaging.

Reporting Summary. Further information on research design is available in the Nature Research Reporting Summary linked to this article.

Data availability
The data that support the findings of this study are available from the corresponding authors upon reasonable request.

References
42. Emre, M. et al. Clinical diagnostic criteria for dementia associated with Parkinson's disease. *Mov. Disord.* **22**, 1689–1707 (2007). quiz 1837.
43. Braak, H., Alafuzoff, I., Arzberger, T., Kretzschmar, H. & Del Tredici, K. Staging of Alzheimer disease-associated neurofibrillary pathology using paraffin sections and immunocytochemistry. *Acta Neuropathol.* **112**, 389–404 (2006).
44. Thal, D. R., Capetillo-Zarate, E., Del Tredici, K. & Braak, H. The development of amyloid beta protein deposits in the aged brain. *Sci. Aging Knowledge Environ.* **2006**, re1 (2006).
45. McKeith, I. G. et al. Diagnosis and management of dementia with Lewy bodies: third report of the DLB Consortium. *Neurology* **65**, 1863–1872 (2005).
46. Alafuzoff, I. et al. Staging/typing of Lewy body related α-synuclein pathology: a study of the BrainNet Europe Consortium. *Acta Neuropathol.* **117**, 635–652 (2009).
47. Alafuzoff, I. et al. Staging of neurofibrillary pathology in Alzheimer's disease: a study of the BrainNet Europe Consortium. *Brain Pathol.* **18**, 484–496 (2008).
48. Thal, D. R. et al. Sequence of Aβ-protein deposition in the human medial temporal lobe. *J. Neuropathol. Exp. Neurol.* **59**, 733–748 (2000).
49. Hyman, B. T. et al. National Institute on Aging–Alzheimer's Association guidelines for the neuropathologic assessment of Alzheimer's disease. *Alzheimers Dement.* **8**, 1–13 (2012).
50. Kovacs, G. G. et al. Aging-related tau astrogliopathy (ARTAG): harmonized evaluation strategy. *Acta Neuropathol.* **131**, 87–102 (2016).
51. Thal, D. R., Griffin, W. S. T., de Vos, R. A. & Ghebremedhin, E. Cerebral amyloid angiopathy and its relationship to Alzheimer's disease. *Acta Neuropathol.* **115**, 599–609 (2008).
52. Nag, S. et al. Hippocampal sclerosis and TDP-43 pathology in aging and Alzheimer disease. *Ann. Neurol.* **77**, 942–952 (2015).
53. Ellisman, M. H., Deerinck, T. J., Shu, X. & Sosinsky, G. E. Picking faces out of a crowd: genetic labels for identification of proteins in correlated light and electron microscopy imaging. *Methods Cell Biol.* **111**, 139–155 (2012).
54. Schindelin, J., Arganda-Carreras, I. & Frise, E. et al. Fiji: an open-source platform for biological-image analysis. *Nat. Methods* **9**, 676–682 (2012).
55. Mastronarde, D. SerialEM A program for automated tilt series acquisition on tecnai microscopes using prediction of specimen position. *Microsc. Microanal.* **9**, 1182–1183 (2003).
56. Hagen, W. J., Wan, W. & Briggs, J. A. Implementation of a cryo-electron tomography tilt-scheme optimized for high resolution subtomogram averaging. *J. Struct. Biol.* **197**, 191–198 (2017).
57. Kremer, J. R., Mastronarde, D. N. & McIntosh, J. R. Computer visualization of three-dimensional image data using IMOD. *J. Struct. Biol.* **116**, 71–76 (1996).
58. Castano-Diez, D., Kudryashev, M., Arheit, M. & Stahlberg, H. Dynamo: a flexible, user-friendly development tool for subtomogram averaging of cryo-EM data in high-performance computing environments. *J. Struct. Biol.* **178**, 139–151 (2012).
59. Navarro, P. P., Stahlberg, H. & Castaño-Díez, D. Protocols for subtomogram averaging of membrane proteins in the Dynamo software package. *Front. Mol. Biol.* **5**, 82 (2018).
60. Denk, W. & Horstmann, H. Serial block-face scanning electron microscopy to reconstruct three-dimensional tissue nanostructure. *PLoS Biol.* **2**, e329 (2004).
61. Ivanova, P. T., Milne, S. B., Byrne, M. O., Xiang, Y. & Brown, H. A. Glycerophospholipid identification and quantitation by electrospray ionization mass spectrometry. *Methods Enzymol.* **432**, 21–57 (2007).
62. Schie, I. W., Krafft, C. & Popp, J. Applications of coherent Raman scattering microscopies to clinical and biological studies. *Analyst* **140**, 3897–3909 (2015).
63. El-Mashtoly, S. F. et al. Automated identification of subcellular organelles by coherent anti-stokes Raman scattering. *Biophys. J.* **106**, 1910–1920 (2014).
64. Baker, M. J. et al. Using Fourier transform IR spectroscopy to analyze biological materials. *Nat. Protoc.* **9**, 1771–1791 (2014).
65. Wrobel, T. P., Wajnchold, B., Byrne, H. J. & Baranska, M. Electric field standing wave effects in FT–IR transflection spectra of biological tissue sections: Simulated models of experimental variability. *Vib. Spectrosc.* **69**, 84–92 (2013).
66. Kallenbach-Thieltges, A. et al. Immunohistochemistry, histopathology and infrared spectral histopathology of colon cancer tissue sections. *J. Biophotonics* **6**, 88–100 (2013).
67. Bassan, P. et al. FTIR microscopy of biological cells and tissue: data analysis using resonant Mie scattering (RMieS) EMSC algorithm. *Analyst* **137**, 1370–1377 (2012).

Corresponding author(s): Henning Stahlberg
Wilma van de Berg
Matthias Lauer

Last updated by author(s): Apr 11, 2019

nature research

Reporting Summary

Nature Research wishes to improve the reproducibility of the work that we publish. This form provides structure for consistency and transparency in reporting. For further information on Nature Research policies, see Authors & Referees and the Editorial Policy Checklist.

Statistics

For all statistical analyses, confirm that the following items are present in the figure legend, table legend, main text, or Methods section.

n/a	Confirmed	
☐	☒	The exact sample size (*n*) for each experimental group/condition, given as a discrete number and unit of measurement
☐	☒	A statement on whether measurements were taken from distinct samples or whether the same sample was measured repeatedly
☒	☐	The statistical test(s) used AND whether they are one- or two-sided *Only common tests should be described solely by name; describe more complex techniques in the Methods section.*
☒	☐	A description of all covariates tested
☒	☐	A description of any assumptions or corrections, such as tests of normality and adjustment for multiple comparisons
☒	☐	A full description of the statistical parameters including central tendency (e.g. means) or other basic estimates (e.g. regression coefficient) AND variation (e.g. standard deviation) or associated estimates of uncertainty (e.g. confidence intervals)
☒	☐	For null hypothesis testing, the test statistic (e.g. *F*, *t*, *r*) with confidence intervals, effect sizes, degrees of freedom and *P* value noted *Give P values as exact values whenever suitable.*
☒	☐	For Bayesian analysis, information on the choice of priors and Markov chain Monte Carlo settings
☒	☐	For hierarchical and complex designs, identification of the appropriate level for tests and full reporting of outcomes
☒	☐	Estimates of effect sizes (e.g. Cohen's *d*, Pearson's *r*), indicating how they were calculated

Our web collection on statistics for biologists contains articles on many of the points above.

Software and code

Policy information about availability of computer code

Data collection	SerialEM (http://bio3d.colorado.edu/SerialEM, Version 3.7), FOCUS (http://focus-em.org, Version 1.1.0). No custom-made software was used.
Data analysis	Image analysis software as described in the manuscript: IMOD (https://bio3d.colorado.edu/imod/, Version 4.9), Dynamo (http://dynamo-em.org, Version 1401), Adobe Photoshop (Version CS6), FIJI/Image J (Version 2.0.0), Amira (Thermo Fischer, Version 6.0). Waters Masslynx and Progeenesis QI (Nonlinear Dynamics, Version 4.0), Matlab (The Mathworks Inc., Versions 9.1-9.4). No custom-made software was used.

For manuscripts utilizing custom algorithms or software that are central to the research but not yet described in published literature, software must be made available to editors/reviewers. We strongly encourage code deposition in a community repository (e.g. GitHub). See the Nature Research guidelines for submitting code & software for further information.

Data

Policy information about availability of data

All manuscripts must include a data availability statement. This statement should provide the following information, where applicable:
- Accession codes, unique identifiers, or web links for publicly available datasets
- A list of figures that have associated raw data
- A description of any restrictions on data availability

Original image data are available from the authors upon reasonable request.

Field-specific reporting

Please select the one below that is the best fit for your research. If you are not sure, read the appropriate sections before making your selection.

☒ Life sciences ☐ Behavioural & social sciences ☐ Ecological, evolutionary & environmental sciences

For a reference copy of the document with all sections, see nature.com/documents/nr-reporting-summary-flat.pdf

Life sciences study design

All studies must disclose on these points even when the disclosure is negative.

Sample size	Data from PDD patients and control patients were used for electron microscopy analysis, as described in Table 1.
Data exclusions	No data were excluded.
Replication	Yes, within the studied patients and the one control patient the results were reliably reproduced.
Randomization	Participants were specifically chosen for this study based on the fulfillment of standard clinical diagnostic criteria for PD, or as aged matched non-demented controls as described in the methods section.
Blinding	Blinding was not relevant as we are describing pathological observations in post-mortem tissue.

Reporting for specific materials, systems and methods

We require information from authors about some types of materials, experimental systems and methods used in many studies. Here, indicate whether each material, system or method listed is relevant to your study. If you are not sure if a list item applies to your research, read the appropriate section before selecting a response.

Materials & experimental systems

n/a	Involved in the study
☐	☒ Antibodies
☒	☐ Eukaryotic cell lines
☒	☐ Palaeontology
☒	☐ Animals and other organisms
☐	☒ Human research participants
☐	☒ Clinical data

Methods

n/a	Involved in the study
☒	☐ ChIP-seq
☒	☐ Flow cytometry
☒	☐ MRI-based neuroimaging

Antibodies

Antibodies used	monoclonal mouse anti-human alpha-Synuclein (clone KM51, Monosan); mouse anti-alpha Synuclein (LB509 concentrate, Invitrogen/180215) detected with Anti-Mouse Ig (Vector/VC-MP-7401), anti-alpha Synuclein (LB509, Abcam/ab27766); VDAC-1/ Porin (Abcam ab14734), LAMP-1 (Abcam ab24170) and S129-phosphorylated α-synuclein (pSer129 Ab 11A5, courtesy of Prothena Biosciences Inc) directly labeled with AlexaFluor 488 were used. Abberior STAR 580 and STAR 635P fluorophores (Abberior, Bioconnect) were used as secondary antibodies. Nuclei were visualized by DAPI staining (Sigma); aSyn FL-140 (Santa Cruz/sc-10717), phospho-S129 (pS129; abcam/ ab59264)
Validation	Commercial antibodies, no validation available/required.

Human research participants

Policy information about studies involving human research participants

Population characteristics	The patient info was anonymized, but Patient genetic profiling as well as classification data are described in the manuscript in Table 1.
Recruitment	Available Parkinson's disease patient tissues from the Netherlands brain bank were used. No selection or exclusion criteria were applied, except that we looked for classical Parkinson's disease or PDD patients without genetic predispositions towards the diseases
Ethics oversight	All donors had given written informed consent for a brain autopsy and the use of the material and clinical information for research purposes. Detailed neuropathological and clinical information was made available, in compliance with the ethical and legal guidelines of the Netherlands Brain Bank (www.brainbank.nl), and all protocols were approved by the local institutional

review board.

Note that full information on the approval of the study protocol must also be provided in the manuscript.

Clinical data

Policy information about clinical studies

All manuscripts should comply with the ICMJE guidelines for publication of clinical research and a completed CONSORT checklist must be included with all submissions.

Clinical trial registration	N/A
Study protocol	N/A
Data collection	N/A
Outcomes	N/A